Sentinel-5p+ Innovation (S5p+I) -Water Vapour Isotopologues (H2O-ISO)

Impact Assessment Report (IAR)

Date:
08.03.2022

Authors:
Iris Thurnherr, Harald Sodemann, Geophysical Institute, University of Bergen, and Bjerknes Center for Climate Research, Bergen, Norway
Matthias Schneider, Christopher Diekmann, Amelie Ninja Röhling and Farahnaz Khosrawi: Institute of Meteorology and Climate Research (IMK-ASF), Karlsruhe Institute of Technology, Karlsruhe, Germany
Tim Trent and Hartmut Bösch: School of Physics and Astronomy, University of Leicester, Leicester and National Centre for Earth Observation NCEO, United Kingdom

Change log

Version	Date	Status	Author	Reason for change
Draft 0.1	**2021-10-26**	initial internal draft for project team	I.Thurnherr, M. Schneider, C. Diekmann, A.N. Röhling, F. Khosrawi, H. Bösch, T. Trent, H. Sodemann	New document
IAR 1.0	**2021-11-30**	Impact assessment report for submission	I.Thurnherr, M. Schneider, C. Diekmann, A.N. Röhling, F. Khosrawi, H. Bösch, T. Trent, H. Sodemann	Including feedback from PM7
IAR 2.0	**2022-03-08**	Impact assessment report, final	I.Thurnherr, M. Schneider, C. Diekmann, A.N. Röhling, F. Khosrawi, H. Bösch, T. Trent, H. Sodemann	Revised report

Contents

1 Purpose and objective

The purpose of this document is to describe the impact assessment of the S5P+I Level-2 products for its added value compared to other datasets of stable water isotopes in water vapour. Based on a detailed description of the used datasets, processing steps, and resulting uncertainties, a strategy for comparing different datasets on even grounds is pursued. Differences between datasets comprise the timing and duration of sampling, the horizontal and vertical coverage, measurement footprint, the sensor principle, and calibration. Model simulations are thereby an important intermediate to assess the scales at which comparisons can ideally be made. Based on the available information, an evaluation of the feasibility of the comparison, the degree of correspondence between different data sets is given. Finally, we derive a set of conclusions and recommendations pertaining to all different aspects of the impact assessment of the S5P+I Level-2 products.

2 Document overview

In Section 3 we present the literature references and a list of the acronyms used throughout this document. Section 4 describes the goals of the impact assessment and a detailed overview of the used datasets is given in Section 5. The impact assessment itself is then presented in Section 6, focusing on the spatial representativeness of the datasets (6.1), the analysis of {H_2O, δD} pair distributions over West Africa (6.2) and the application of δD and H_2O in data assimilation (6.3). The conclusions are given in Section 7 and an outlook in Section 8.

3 References, terms and acronyms

3.1 References

Berthou S., Rowell, D. P., Kendon, E. J., Roberts, M. J., Stratton, R. A., Crook, J. A., and Wilcox, C.,2019: Improved climatological precipitation characteristics over West Africa at convection-permitting scales. Climate Dynamics, 53(3-4), 1991–2011, https://doi.org/10.1007/s00382-019-04759-4.

Cauquoin, A., and Werner, M., 2021: High-resolution nudged isotope modeling with ECHAM6-wiso: Impacts of updated model physics and ERA5 reanalysis data, Journal of Advances in Modeling Earth Systems, 13, e2021MS002532, https://doi.org/10.1029/2021MS002532.

Chazette, P., Flamant, C., Sodemann, H., Totems, J., Monod, A., Dieudonné, E., Baron, A., Seidl, A., Steen-Larsen, H. C., Doira, P., Durand, A., and Ravier, S., 2021: Experimental investigation of the stable water isotope distribution in an Alpine lake environment (L-WAIVE), Atmos. Chem. Phys., 21, 10911–10937, https://doi.org/10.5194/acp-21-10911-2021.

Crook, J., Klein, C., Folwell, S., Taylor, C. M., Parker, D. J., Stratton, R., & Stein, T., 2019: Assessment of the representation of West African storm lifecycles in convection-permitting simulations, Earth and Space Science, 6, 818– 835, https://doi.org/10.1029/2018EA000491.

Dhonneur, G., 1981: Les amas nuageux mobiles, principale composante de la météorologie du Sahel, La Météorologie Paris, 6(27), 75–82.

Diekmann, C. J., Schneider, M., Knippertz, P., de Vries, A. J., Pfahl, S., Aemisegger, F., et al., 2021a: A Lagrangian perspective on stable water isotopes during the West African Monsoon, Journal of Geophysical Research: Atmospheres, 126, e2021JD034895, https://doi.org/10.1029/2021JD034895.

Diekmann, C. J., Schneider, M., Ertl, B., Hase, F., García, O., Khosrawi, F., Sepúlveda, E., Knippertz, P., and Braesicke, P., 2021b: The MUSICA IASI {H_2O, δD} pair product, Earth Syst. Sci. Data Discuss. [preprint], https://doi.org/10.5194/essd-2021-87, in review.

Eckstein, J., Ruhnke, R., Pfahl, S., Christner, E., Diekmann, C., Dyroff, C., Reinert, D., Rieger, D., Schneider, M., Schröter, J., Zahn, A., and Braesicke, P., 2018: From climatological to small-scale applications: simulating water isotopologues with ICON-ART-Iso (version 2.3), Geosci. Model Dev., 11, 5113–5133, https://doi.org/10.5194/gmd-11-5113-2018.

Fink, A. H., Vincent, D. G., and Ermert, V., 2006: Rainfall types in the West African Sudanian zone during the summer monsoon 2002, Monthly Weather Review, 134(8), 2143–2164, https://doi.org/10.1175/MWR3182.1.

Galewsky, J., Steen-Larsen, H. C., Field, R. D., Worden, J., Risi, C., and Schneider, M., 2016: Stable isotopes in atmospheric water vapor and applications to the hydrologic cycle, Rev. Geophys., 54, 809– 865, https://doi.org/10.1002/2015RG000512.

Huffman, G., Bolvin, D., Nelkin, E., and Tan, J., 2019: Integrated Multi-satellitE Retrievals for GPM (IMERG) Technical Documentation. Technical report, NASA Goddard Centre. https://gpm.nasa.gov/data/imerg, accessed on 2021-02-15.

Kanamitsu, M., Kumar, A., Juang, H.-M. H., Schemm, J.-K., Wang, W., Yang, F., Hong, S.-Y., Peng, P., Chen, W., Moorthi, S., and Ji, M., 2002: NCEP dynamical seasonal forecast system 2000, Bulletin of the American Meteorological Society, 83, 1019–1037, https://doi.org/10.1175/1520-0477(2002)083<1019:NDSFS>2.3.CO;2.

Khosrawi, F., Toride, K., Yoshimura, K., Diekmann, C. J., Ertl, B., Hase, F., and Schneider, M., 2021: Can the assimilation of water isotopologue observation improve the quality of tropical diabatic heating and precipitation?, Weather Clim. Dynam. Discuss. [preprint], https://doi.org/10.5194/wcd-2021-49.

Knippertz, P., Fink, A. H., Deroubaix, A., Morris, E., Tocquer, F., Evans, M. J., Flamant, C., Gaetani, M., Lavaysse, C., Mari, C., Marsham, J. H., Meynadier, R., Affo-Dogo, A., Bahaga, T., Brosse, F., Deetz, K., Guebsi, R., Latifou, I., Maranan, M., Rosenberg, P. D., and Schlueter, A., 2017: A meteorological and chemical overview of the DACCIWA field campaign in West Africa in June-July 2016, Atmos. Chem. Phys., 17(17):10893–10918, doi: 10.5194/acp-17-10893-2017.

Marsham, J. H., Dixon, N., Garcia-Carreras, L., Lister, G. M. S., Parker, D. J., Knippertz, P., and Birch, C., 2013: The role of moist convection in the West African monsoon system: Insights from continental-scale convection-permitting simulations, Geophys. Res. Lett., 40, 1843– 1849, https://doi.org/10.1002/grl.50347.

Martínez, I. R., & Chaboureau, J., 2018: Precipitation and Mesoscale Convective Systems: Explicit versus Parameterized Convection over Northern Africa, Monthly Weather Review, 146(3), 797-812, https://doi.org/10.1175/MWR-D-17-0202.1

Maurer, V., Bischoff-Gauß, I., Kalthoff, N., Gantner, L., Roca, R. and Panitz, H.-J., 2017: Initiation of deep convection in the Sahel in a convection-permitting climate simulation for northern Africa, Q.J.R. Meteorol. Soc., 143: 806-816. https://doi.org/10.1002/qj.2966.

O'Dell, C. W., Connor, B., Bösch, H., O'Brien, D., Frankenberg, C., Castano, R., Christi, M., Eldering, D., Fisher, B., Gunson, M., McDuffie, J., Miller, C. E., Natraj, V., Oyafuso, F., Polonsky, I., Smyth, M., Taylor, T., Toon, G. C., Wennberg, P. O., and Wunch, D., 2012: The ACOS CO_2 retrieval algorithm – Part 1: Description and validation against synthetic observations, Atmos. Meas. Tech., 5, 99–121, https://doi.org/10.5194/amt-5-99-2012.

Pante, G., Knippertz, P., 2019: Resolving Sahelian thunderstorms improves mid-latitude weather forecasts. Nat Commun 10, 3487, https://doi.org/10.1038/s41467-019-11081-4.

Schneider, M., Wiegele, A., Barthlott, S., González, Y., Christner, E., Dyroff, C., García, O. E., Hase, F., Blumenstock, T., Sepúlveda, E., Mengistu Tsidu, G., Takele Kenea, S., Rodríguez, S., and Andrey, J., 2016: Accomplishments of the MUSICA project to provide accurate, long-term, global and high-resolution observations of tropospheric {H_2O,δD} pairs – a review, Atmos. Meas. Tech., 9, 2845–2875, https://doi.org/10.5194/amt-9-2845-2016.

Schneider, M., Ertl, B., Diekmann, C. J., Khosrawi, F., Weber, A., Hase, F., Höpfner, M., García, O. E., Sepúlveda, E., and Kinnison, D., 2021a: Design and description of the MUSICA IASI full retrieval product, Earth Syst. Sci. Data Discuss. [preprint], https://doi.org/10.5194/essd-2021-75, in press.

Schneider, M., Ertl, B., Diekmann, C. J., Khosrawi, F., Röhling, A. N., Hase, F., Dubravica, D., García, O. E., Sepúlveda, E., Borsdorff, T., Landgraf, J., Lorente, A., Chen, H., Kivi, R., Laemmel, T., Ramonet, M., Crevoisier, C., Pernin, J., Steinbacher, M., Meinhardt, F., Deutscher, N. M., Griffith, D. W. T., Velazco, V. A., and Pollard, D. F., 2021b: Synergetic use of IASI and TROPOMI space borne sensors for generating a tropospheric methane profile product, Atmos. Meas. Tech. Discuss. [preprint], https://doi.org/10.5194/amt-2021-31, in review.

Sultan, B., & Janicot, S., 2003: The West African Monsoon Dynamics. Part II: The "Preonset" and "Onset" of the Summer Monsoon, Journal of Climate, 16(21), 3407-3427, https://doi.org/10.1175/1520-0442(2003)016<3407:TWAMDP>2.0.CO;2.

Toride, K., Yoshimura, K., Tada, M., Diekmann, C., Ertl., B., Khosrawi, F., and Schneider, M., 2021: Potential of mid-tropospheric water vapor isotopes to improve large-scale circulation and weather predictability, Geophysical Research Letters, 48, e2020GL091 698, https://doi.org/10.1029/2020GL091698.

Trent, T., Boesch, H., Somkuti, P. and Scott, N.A., 2018: Observing water vapour in the planetary boundary layer from the short-wave Infrared, Remote Sensing, 10(9), p.1469, https://doi.org/10.3390/rs10091469.

Vergara-Temprado, J., Ban, N., Panosetti, D., Schlemmer, L., and Schär, C., 2020: Climate Models Permit Convection at Much Coarser Resolutions Than Previously Considered, Journal of Climate, 33(5), 1915-1933. https://doi.org/10.1175/JCLI-D-19-0286.1.

Yoshimura, K., Miyoshi, T., and Kanamitsu, M., 2014: Observing system simulation experiments using water vapour isotope information, Journal of Geophysical Research, 119, 7842–7862, https://doi.org/10.1002/2014JD021662.

Zängl, G., Reinert, D., Rípodas, P. and Baldauf, M., 2015: The ICON (ICOsahedral Non-hydrostatic) modelling framework of DWD and MPI-M: Description of the non-hydrostatic dynamical core, Q.J.R. Meteorol. Soc., 141, 563-579., https://doi.org/10.1002/qj.2378.

3.2 Applicable Documents

[AD1] Requirements Baseline Document (RB). https://s5pinnovationh2o-iso.le.ac.uk/wp-content/uploads/2019/11/RBD_S5pI_H2O_ISO_v1.1.pdf. Date: 2020-09-29

[AD2] Algorithm Theoretical Basis Document (ATBD). https://s5pinnovationh2o-iso.le.ac.uk/wp-content/uploads/2021/02/S5P-I_ISO_ATBD_Version1.3.pdf. Date: 2020-09-29

[AD3] Auxiliary User Manual (AUM). https://s5pinnovationh2o-iso.le.ac.uk/wp-content/uploads/2020/06/aum_s5p-i_iso_version_1.3.pdf. Date 2021-08-13

[AD4] Validation Report (VR). https://s5pinnovationh2o-iso.le.ac.uk/wp-content/uploads/2021/10/S5p-I_VR_Version1.3.pdf. Date 2021-10-19

3.3 Terms, definitions and abbreviated terms

The most important symbols, acronyms and abbreviations related to the data product of this document are described in this subsection.

COSMOiso	Isotope enabled Consortium for Small-scale Modeling model
CTRL	Reference assimilation experiment
DACCIWA	Dynamics-Aerosol-Chemistry-Cloud Interactions in West Africa
ECHAM5-wiso	Isotope-enabled version of the fifth-generation ECHAM model
ECHAM6-wiso	Isotope-enabled version of the sixth-generation ECHAM model
ECPC	Experimental Climate Predictions Center
ERA5	Newest generation ECMWF reanalysis dataset
ERA-interim	ECMWF reanalysis dataset, available from 1.1.1979 until 31.12.2019
GPM	Global Precipitation Measurement
GSM	Global Spectral Model
IASI	Infrared Atmospheric Sounding Interferometer
ICON-ARTiso	Isotope-enabled version of the model ICON
IFS	Integrated Forecasting System (global numerical weather prediction system)
IMERG	Integrated Multi-satellitE Retrievals for GPM
IsoGSM	Isotope-Incorporated Global Spectral Model
LETKF	Local Ensemble Transform Kalman Filter
LUT	Loop-Up Table
L-WAIVE	Lacustrine-Water vApor Isotope inVentory Experiment
MUSICA	Multi-platform remote Sensing of Isotopologues for investigating the Cycle of Atmospheric water
NCEP	National Centers for Environmental Prediction
NWP	Numerical Weather Prediction
OSSE	Observation System Simulation Experiment
PREPBUFR	PREProcessed and quality-controlled observations of the Binary Universal Form for the Representation of meteorological data
RMSD	Root Mean Square Deviation
S5P	Sentinel-5p
TROPOMI	Tropospheric Monitoring Instrument
WAM	West African Monsoon

4 Goals of data assessment

We specify the following goals for this IAR:

1. We assess how well in-situ measurements represent the large-scale spatial δD pattern. More specifically, we ask the question, on which length and time scale in-situ measurements can be compared to satellite retrievals, and how this depends on the large-scale weather situation. Similarly, we consider up to or at which height should in situ measurements be done to ensure a good comparison with the satellite data. Based on these questions, we address to what extent in-situ measurements are complementary rather than overlapping with satellite measurements.

2. We assess the information offered by the new S5P isotopologue total column data for West Africa in addition to the already available MUSICA IASI free tropospheric isotopologue data. Specifically, we estimate the impact in West Africa of a boundary layer water vapour isotopologue product (combining the S5P total column data with the MUSICA IASI free tropospheric data offers the potential for generating a boundary layer data product by applying the method proposed in Schneider et al., 2021b).

3. Finally, we provide a preliminary investigation of the impact of the S5P water isotope in the context of atmospheric data assimilation.

4. Overall, we have the goal to assess the additional value of S5P satellite data compared to other satellite data, in-situ measurements, and model simulations.

5 Data

To assess the impact of the TROPOMI stable water vapour isotopologues product a variety of datasets are used in this report. In addition to total and subcolumn δD retrievals from the TROPOMI measurements (Sec. 5.1), we use measurements of in situ vertical δD profiles from the L-WAIVE campaign in June 2019 (Sec. 5.2), the MUSICA IASI stable water isotopologues product (Sec. 5.3) and model simulations with the isotope-enabled numerical weather prediction (NWP) models $\text{COSMO}_{\text{iso}}$ and ICON-ART-Iso (Sec. 5.4). The wide range of spatial and temporal resolutions of these datasets allows to assess the representativeness of the S5P δD retrievals on various spatial and temporal scales and to develop recommendations for in situ measurement-satellite-model δD comparison studies. Furthermore, the high spatial resolution of the S5P dataset allows to validate the simulation of spatial δD patterns on a synoptic scale and thereby can potentially contribute to a process-based understanding of shortcomings in the representation of the atmospheric water cycle in NWP models.
In the following, the datasets and methods used in the IAR are described.

5.1 S5P total and sub-column retrievals

This study makes use of version 1 of the TROPOMI stable water vapour istopologue L2 prototype product. Full details of the TROPOMI product algorithm are outlined in AD2, with product performance given in AD4.

For comparisons to the $\text{COSMO}_{\text{iso}}$ simulations direct comparisons can be made to the total column TROPOMI water vapour information (e.g. XH_2O, XHDO, XδD) using a pressure weighting function h, calculated following equation A5 in O'Dell et al. 2012 using the $\text{COSMO}_{\text{iso}}$ output fields:

$$XH2O_{pwf} = \boldsymbol{h}^t \boldsymbol{x}_t, \tag{1}$$

where x_t is the reference H_2O profile (in ppm) in the $\text{COSMO}_{\text{iso}}$ simulation. The same step is then done for XHDO before calculating the pressure-weighted total column value $\text{X}\delta\text{D}_{\text{pwf}}$:

$$\text{X}\delta\text{D}_{pwf} = \left(\frac{XHDO_{pwf}}{XH2O_{pwf}} R_s^{-1} - 1\right) \cdot 10^3, \tag{2}$$

where R_s is a standard isotopic ratio as defined by the IAEA.

For comparison with the satellite retrievals, in-situ vertical profiles of δD measured from an ultra-light aircraft are available from the L-WAIVE campaign (see Section 5.2). Due to the unique nature of these profiles, this study is also able to examine the performance of the TROPOMI sub-column near to the surface. In the first instance TROPOMI pixels were collocated in time and space with the L-WAIVE dataset. For five satellite overpasses, δD retrievals are available close to the campaign site from 12 to 22 June 2019 (Fig. 1). To facilitate this comparison, a new sub-column dataset was generated of collocated TROPOMI pixels based on the height of the L-WAIVE profiles. For TROPOMI this involves setting all levels above the sub-column height to zero in the pressure weighting function (h_s) and then recalculating the column for both XH_2O and XHDO. These are in turn then used to calculate the new sub-column XδD. For sub-column comparisons to L-WAIVE a new column averaging kernel is needed that removes all correlations in levels above the sub-column. Here we use the same approach as outlined in RD1, by applying the augmented pressure weighting function (h_s) to the 2D averaging kernel (**A**):

$$a_{hs} = \boldsymbol{h}_s \boldsymbol{A} \boldsymbol{h}_s^T, \tag{3}$$

where a_{hs} is the sub-column averaging kernel normalised by the pressure weighting function. The global product column averaging kernels are provided via a look-up table (LUT) which uses the geometric air mass factor to interpolate across the LUT. For this study the LUT was updated to include sub-columns based on a range of levels from the upper troposphere to the near-surface covering the vertical extent of the in-situ profiles. New column averaging kernels (a_{hs}) were then produced for each TROPOMI pixel in the match-up data set and provided along with the corresponding updated pressure weighting functions. Calculation of sub-columns ($XH2O_{est}$) can then be performed as given in the following equation:

$$XH2O_{est} = \boldsymbol{h}_s^T \boldsymbol{x}_a + \boldsymbol{a}_{hs}(\boldsymbol{x}_t - \boldsymbol{x}_{as}), \tag{4}$$

where $\boldsymbol{x}_{as}$ is the a priori H_2O subcolumn profile. It should be noted that the column averaging kernels in the file are normalised by h_s, for use in this context they are scaled by the pressure weighting function used for calculating the subcolumn amount. The subcolumn retrievals for the collocated satellite overpasses are shown in Fig. 1.

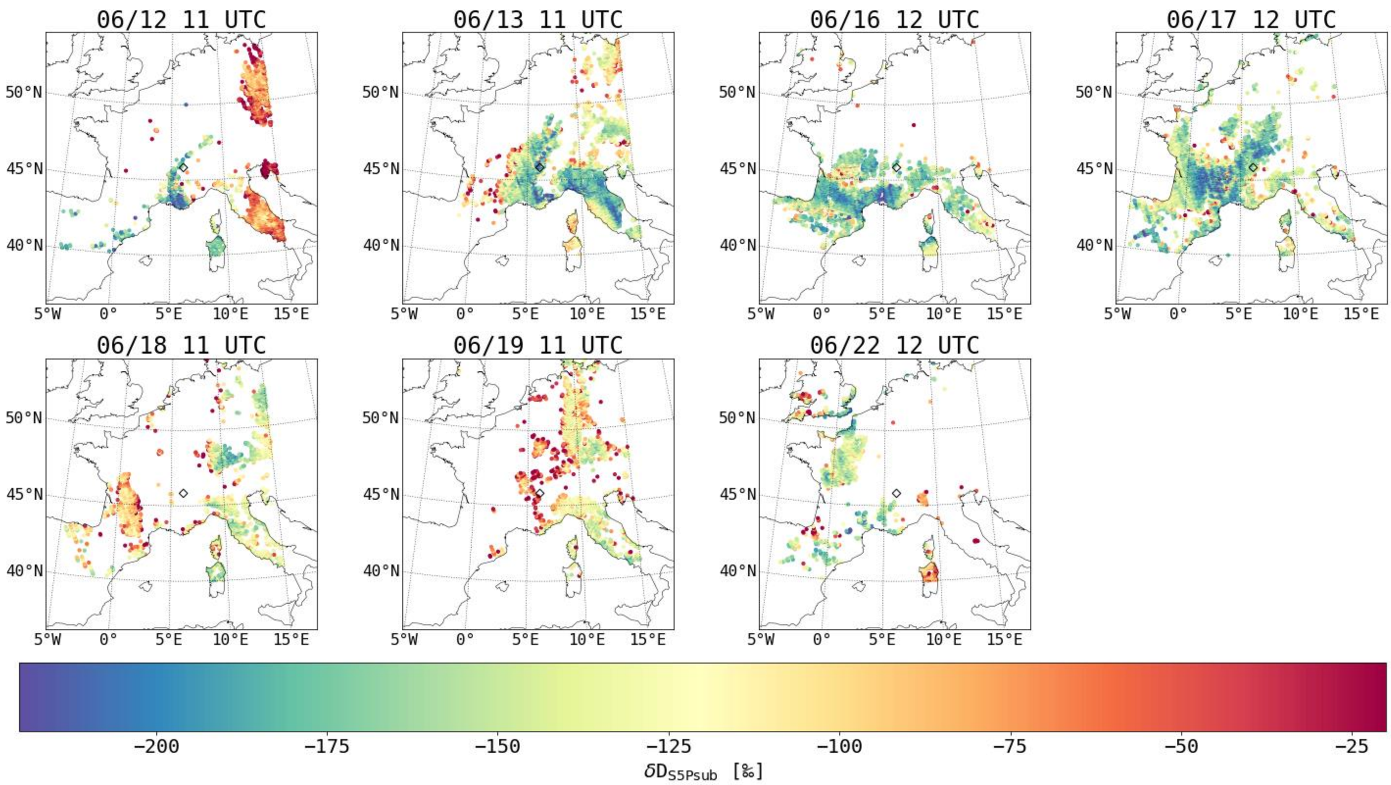

Figure 1: Subcolumn δD retrievals for satellite overpasses during the L-WAIVE campaign in June 2019. The location of the L-WAIVE campaign is indicated with a black diamond.

5.2 In-situ profiles from L-WAIVE campaign

The Lacustrine-Water vApor Isotope inVentory Experiment (L-WAIVE) field campaign took place in June 2019 in the Annecy valley in the French Alps. The L-WAIVE campaign was the first of several validation campaigns as part of the LEMON project (https://lemon-dial-project.eu/) that aims to develop a Lidar emitter for space applications. The main objective of L-WAIVE was the measurement of vertical isotope profiles over Lake Annecy to study the heterogeneity of stable water isotopes in the lower troposphere. During this campaign, a Picarro laser spectrometer L2130-i was installed on an ultralight aircraft to continuously measure the isotopic composition of atmospheric water vapour. The raw measurements of the isotope parameters were corrected for the humidity dependency and calibrated across the campaign period following recommendations from the International Atomic Energy Agency (for details see Chazette et al., 2021). A total of 11 flights were performed during the one week period from 13 to 20 June, providing vertical profiles of δD in water vapour one or two times a day (Fig. 2). The profiles are filtered for rapid elevation changes and periods of relative humidity above 90% indicating in-cloud measurements. The measurements are available at 10s temporal resolution and reach up to 3500 m above surface. During the L-WAIVE campaign, satellite overpasses occurred daily around noon. For five of these overpasses, δD retrievals are available close to the campaign site from 12 to 22 June 2019 (Fig. 1).

In September 2021, similar air-borne measurements were conducted in the Rhone valley at Aubenas (F). These measurements are not yet available and can be used in future comparison studies of in situ vertical profiles with satellite retrievals.

For comparison with the S5P subcolumn retrievals, the vertical profiles are sampled at the pressure levels of the S5P subcolumn retrievals +- 5hPa and the pressure weighting function and subcolumn kernel of pixels of nearby satellite overpasses are applied following equation 16 in Trent et al. (2018). This procedure provides pseudo subcolumn δD retrievals from the vertical profiles (see Sec. 6.1.3).

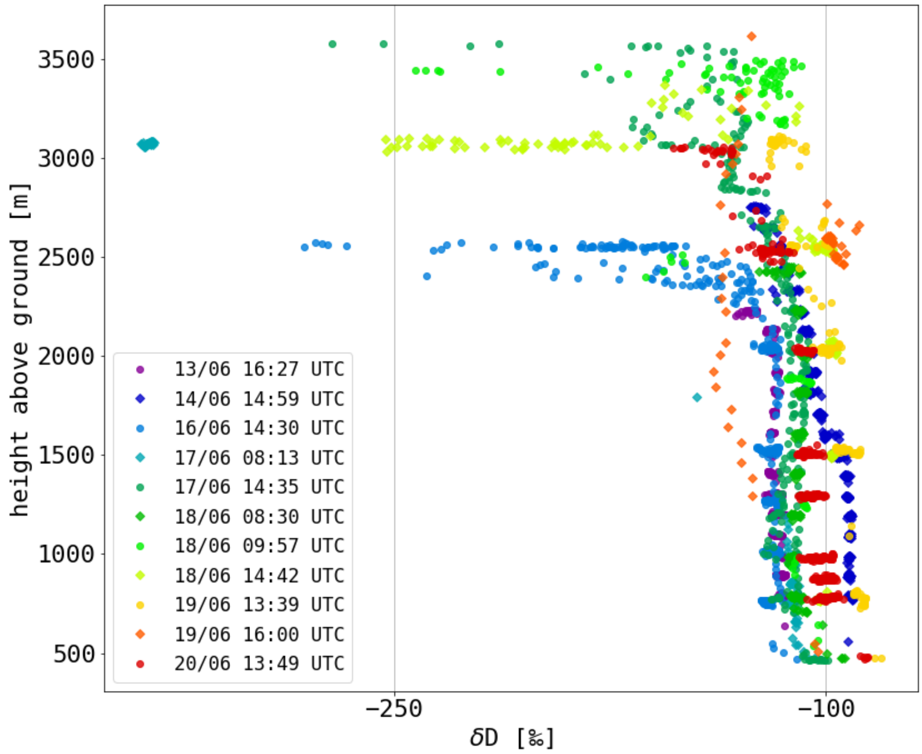

Figure 2: Overview of in situ δD profiles measured during the L-WAIVE campaign in June 2019 coloured by the start time of the flights.

5.3 MUSICA IASI data

To assess the impact of the S5P water isotope data over West Africa, the global and daily remotely sensed {H_2O, δD} pair dataset based on Metop/IASI measurements is used (Schneider et al., 2021a; Diekmann et al., 2021b; see [AD1]). This {H_2O, δD} pair product has the main focus on water vapour abundances in the mid-troposphere (around 600 hPa) and is available for cloud-free scenes over land and ocean. Its full data availability ranges from October 2014 to December 2020 with two global maps of {H_2O, δD} pair data per day (according to the overpass times of 09.30 and 21.30 local time). The full dataset is referenced via the DOI: https://dx.doi.org/10.35097/415.

5.4 Simulation data sets

Isotope-enabled NWP models, such as $COSMO_{iso}$ and ICON-ART-Iso, provide stable water isotopologues datasets with a high spatial and temporal coverage which give detailed insights into atmospheric processes along the water cycle. To evaluate the performance of these models, measurements of stable water isotopologues, as for example provided by satellite retrievals or in-situ measurements, are needed. The S5P isotopologues dataset provides unique high resolution data to compare to isotope-enabled NWP prediction models and evaluate the representation of the atmospheric water cycle in these models.

5.4.1 $COSMO_{iso}$ simulations at high and middle latitudes

Two 7-day $COSMO_{iso}$ simulations starting at 00 UTC on 12 June 2019 (referred to as CI_{12} in the following) and 00 UTC on 15 June 2019 (referred to as CI_{15} in the following) were conducted to cover the L-WAIVE campaign period from 12 to 22 June 2019. These simulations were performed with a spatial resolution of 0.1° on 40 vertical levels and explicit convection. The consideration of an explicit convection setup relies on Vergara-Temprado et al. (2020), who stated that for a horizontal grid spacing below 25 km switching off the parameterization of deep convection leads to overall better results than increasing the horizontal resolution. They were initialised and driven at the lateral boundaries by output from an ECHAM6-wiso simulation (Cauquoin et al., 2021). The ECHAM6-wiso output is available in 6-hourly temporal resolution and a spatial resolution of *0.5°* on 95 vertical levels and was nudged to ERA5 reanalyses. The model domain of the $COSMO_{iso}$ simulations covers Western Europe including parts of the Atlantic Ocean, Mediterranean, Baltic and Nordic Sea (see Fig. 3).

For a comparison of the simulated δD distribution with the S5P δD retrievals, pseudo total column profiles are calculated from the COSMOiso output fields (see Section 5.1).

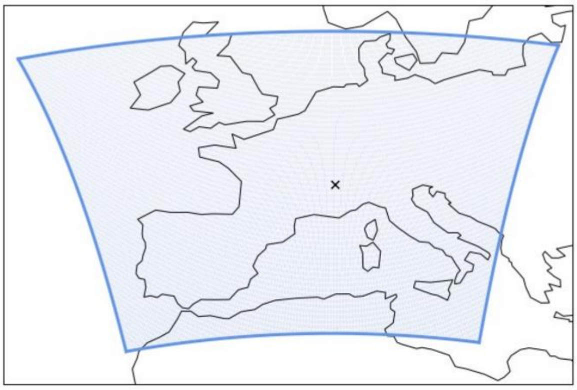

Figure 3: COSMO$_{iso}$ domain for the 7-day forecasts. The black cross marks the location of the measurement site during the L-WAIVE campaign.

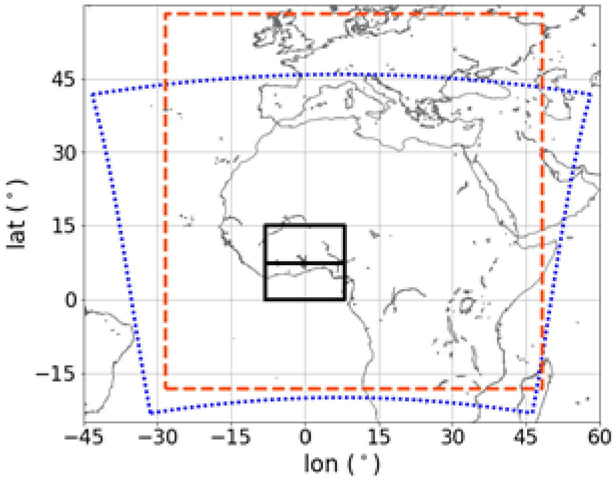

Figure 4: Domains considered for the impact assessment of S5P data over West Africa. The blue dotted frame marks the COSMO$_{iso}$ model domain, the red dashed frame the ICON-ARTiso domain and the two black boxes indicate the target regions over the Sahel (upper box) and the Guinea Coast (lower box)

5.4.2 COSMO$_{iso}$ simulations for the Sahel zone

Another high-resolution, nudged simulation with COSMO$_{iso}$ aims to address the impact assessment of the S5P data with focus on West Africa (Region of Interest 2) during the WAM season 2016. This simulation was performed and provided by Andries de Vries (ETH, Zurich) and the time period was chosen to match the DACCIWA campaign (01 June-31 July 2016; Knippertz et al., 2017). The simulation period is June – September 2016 to cover the West African Monsoon, and the model output frequency was set to 1 h. Data provided by the global isotope-enabled model ECHAM5 wiso are used as initial and boundary conditions as well as for a spectral nudging of the horizontal wind fields above 850 hPa. This serves to keep the meteorology close to reality, as the ECHAM5-wiso simulation was nudged to ERA-interim reanalyses provided by ECMWF. The model domain of the COSMO$_{iso}$ simulations is chosen such that it covers the dominant moisture source regions of the

WAM (see Fig. X1). The model has 40 vertical hybrid levels between the surface and 22.7 km and a horizontal grid spacing of 14 km (similar to the horizontal pixel size of Metop/IASI data). Similar to the simulation described in Sect. 5.4.1, again an explicit convection setup is employed. Specifically for the WAM, various studies reported significant improvements when using explicit convection (Marsham et al., 2013; Maurer et al., 2017; Martínez and Chaboureau, 2018; Berthou et al., 2019; Crook et al., 2019; Pante and Knippertz, 2019).

5.4.3 ICON-ART-Iso simulation for one full year

In addition to the $COSMO_{iso}$ simulation over West Africa, a simulation with the global isotope-enabled ICON-ART iso serves to provide model-based {H_2O, δD} pair data with a quasi-climatological scope. This simulation employs a global grid with a horizontal grid size of 80 km and with 90 vertical hybrid levels from the surface up to 75 km. Additionally, it incorporates a refined and two-way-interacting nest that covers West Africa (see Fig. 4). The simulation for the nested domain uses a 40 km grid with 60 vertical hybrid levels up to 22 km. A free-running simulation setup is chosen, with a 3-year target period between 2017–2019 and model output generated once per day (at 12 UTC, in agreement with the local overpass times of S5p over West Africa). Operational reanalysis data of the Integrated Forecasting System (IFS) from ECMWF are used for initialising the meteorological state, including water vapor, liquid and frozen cloud and rain water. The initialisation of the moist variables specific for HDO is coupled to the initial H_2O state by considering climatological values of δD and applying those to the ICON fields. This includes three global mean δD values for water vapor (troposphere, tropopause and stratosphere) and one for the hydrometeors (Eckstein et al., 2018). To minimise the influence of this rough δD initialisation, a spin-up time of 6 months is considered, i.e. each simulation is initialised on the 22 June 2016. As the horizontal resolution is far from resolving convection explicitly, the convection is computed via the parameterized schemes for deep and shallow convection (Zängl et al., 2015). Sea surface temperatures and sea ice cover are interpolated on a daily basis from monthly climatologies provided by the AMIP II project (Eckstein et al., 2018).

5.4.4 Assimilation studies using the model IsoGSM

The assimilation experiments are performed with the isotope-incorporated Global Spectral Model (IsoGSM). This model is based on the Scripps Experimental Climate Predictions Center's (ECPC) Global Spectral Model (GSM) that has been used by NCEP to perform operational analyses and medium-range forecasts (Kanamitsu et al., 2002). We use an IsoGSM ensemble simulation (size 96) performed with a T62 horizontal resolution (about 1.9° x 2°, 200 x 200 km) and 28 vertical sigma levels from the surface up to 2.5 hPa.

The data assimilation is performed with a Local Ensemble Transform Kalman Filter (LETKF). To investigate the potential impact of the assimilation of S5P data or of S5P and IASI data together on the meteorological analyses Observation System Simulation Experiment (OSSE) are performed. In an OSSE, a model simulation is regarded as "truth" ("Nature run") and several data assimilation experiments with synthetic observations derived from the Nature run are conducted that aim to reproduce the Nature run as closely as possible. The synthetic data mocks therefore the data that would be obtained if satellites or ground-based sensors were actually operated (Yoshimura et al., 2014). For generating the synthetic S5P and MUSICA IASI (Metop A and B) data set the spatial coverage and the observational error statistics of the real data are used. For the S5P observations, vertically integrated water vapour (q) and water vapour isotopes (δD) has been used with the same geographical coverage as for IASI, but over land only. For the observational errors, for δD the same error as for IASI has been assumed and for S5P q an error of 1 kg m^{-2} has been assumed.

The Nature run is generated by an IsoGSM simulation over two years, covering the time period from 2015 to 2016. This time period has been chosen to match the $COSMO_{iso}$ simulations over West Africa during the DACCIWA campaign (see Sec. 5.4.2). The same results are expected with OSSEs for years covering the availability of S5P data. The model run has been started on 1 June 2015 at 00 UTC. The first year has been discarded as spin-up period to minimise the possibility of the model's drift. The initial conditions for the 96 ensemble members were taken from the Nature run. The first initialisation was done on 1 June 2016 at 00 UTC and then all other ensemble members were initialised with the following consecutive 6-hour time steps. Therefore, the initial conditions can be considered as being independent from the Nature run but representing similar climatological conditions. The following two months, thus from 1 July 2016 to 1 September 2016 have then been used as the experimental period and the results of our assimilation experiments are then evaluated for the latter one-month period (1 August to 31 August 2016). Similar results than the ones derived here for 2016 can be expected for any other year.

The synthetic conventional observations (radiosondes, wind profilers, aircrafts, ships, buoys, surface stations, and wind data derived from satellites and radar) are generated based on a data set used in the NCEP operational system (known as PREPBUFR, i.e. preprocessed and quality controlled observations of the Binary Universal Form for the Representation of meteorological data (BUFR), https://rda.ucar.edu/datasets/ds337.0/). The conventional observations are temporally and spatially resampled to the IsoGSM grid every 6-hours. For the data assimilation a multiplicative inflation is used with a inflation parameter of 1.05 to maintain an appropriate ensemble spread and to avoid filter divergence. The horizontal localisation scale is set to be 500 km (influence radius of 1826 km for best assimilation performance; Toride et al., 2021).

6 Impact assessment

6.1 Analysis of temporal and spatial scales

δD in atmospheric water vapour can be studied using a variety of observational platforms, that have a wide range of spatial and temporal resolutions. While satellite-retrieved products of δD in water vapour allow to study δD variability on spatial scales of several 1000 km every 12-24 h, the few available in-situ water vapour measurements of δD are at a much higher temporal resolution (seconds) and cover a more limited spatial extent (10s of km). To compare these different datasets to each other, and to model simulations, the dominant time and length scales of water vapour δD features in different parts of the atmosphere need to be identified and taken into account. In the first part of the impact assessment (Sec. 6.1.1), we therefore analyse the spatial and temporal representativeness of all involved datasets. The intention of such a procedure is to obtain an unbiased comparison of the different datasets on even grounds. Based on such a careful setup, we can draw more firm and general recommendations for future comparison studies of in-situ measurement, satellite products, and model-simulated δD. Due to large spatial and temporal coverage of the $COSMO_{iso}$ dataset, these model simulations are used to create a general understanding of the main temporal and spatial scales of δD in water vapour (Sec. 6.1.1). Based on the scales identified within the model representations of the atmosphere, the datasets are compared thereafter (Sec. 6.1.2).

6.1.1 Spatial and temporal scales of δD in total column water vapour

Two statistical measures are used to analyse the spatial scales of δD in the two $COSMO_{iso}$ simulations: (i) the Pearsons correlation is used to study correlation in time of two points in the $COSMO_{iso}$ domain. (ii) The root mean square deviation (RMSD) will give additional information on the offset in δD between two grid points. The combination of these two measures enables to take relative and absolute changes in δD into account.

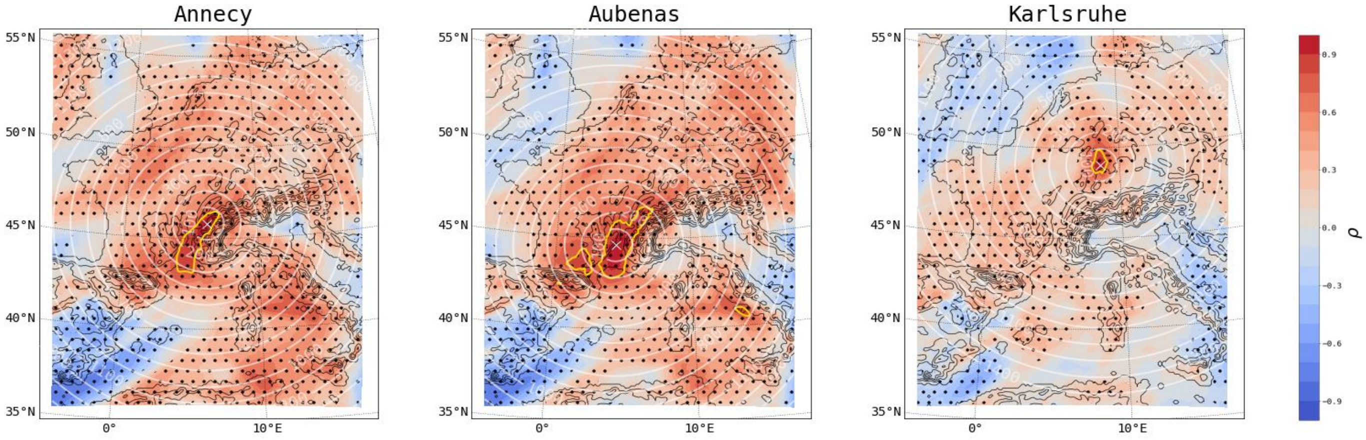

Figure 5: (left) Map of Pearson correlation coefficient ρ between the time series of $X\delta D_{pwf}$ at Annecy (left), Aubenas (middle) and Karlsruhe (right) and any point in the $COSMO_{iso}$ domain for simulation CI_{12}. White contours show the distance in 100 km steps. Black contours show the topography.

Fig. 5 shows the Pearson correlation coefficient ρ for 5-day time series of $X\delta D_{pwf}$ at Annecy (F), the location of the L-WAIVE campaign, Aubenas (F), which is the location of a field campaign in 2021 and a potential site for future satellite-in-situ measurement comparisons, and Karlsruhe (DE), which represents a location in flat terrain, correlated with any other point in the domain for CI_{12}. These three locations are chosen to demonstrate how the variability of correlation patterns depends on the local topography. To highlight the areas of highest correlation, ρ=0.8 is marked in yellow. In Annecy, there is a relatively large area of ρ above 0.8 spreading along the Western Alps towards the Mediterranean Sea in CI_{12}. For Aubenas, the shape of the 0.8 contour line is similar to Annecy, but covers a larger area between the Massif Central and the Western Alps. The regions of high correlation with the L-WAIVE or Aubenas location follow closely the local topography, where the Alpine mountain ridge forms the Southeastern edge. In Karlsruhe, the area of high correlation is more symmetric around the origin and covers an area of less than 100 km distance from the reference point. Due to the absence of topographic barriers around Karlsruhe, δD patterns are less strongly topographically forced and, thus, show high variability over a short distance. This is in contrast to the strong topographic forcing in Annecy and Aubenas, which leads to a non-symmetric region of high correlation and a weaker and more variable decrease in ρ with distance from the reference location (Δd) (Fig. 6) than seen in Karlsruhe. In addition, the influence of different weather systems at the two locations during the simulation period may have influenced the correlation patterns. It is an important conclusion from this analysis that the correlation scales are varying in space and time on synoptic scales (see below).

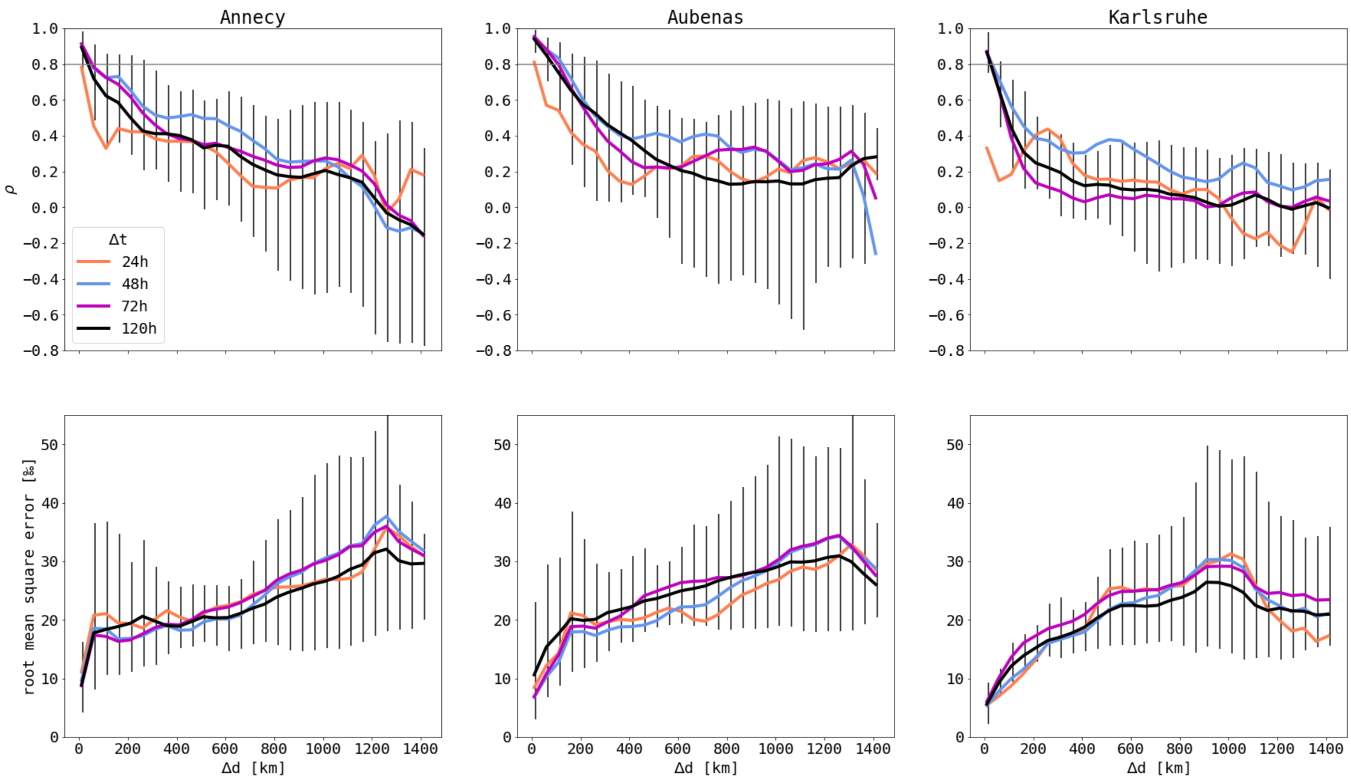

Figure 6: Mean and 5-95 percentile range of ρ (top) and RMSD (bottom) for δD_{pwf} binned to distances from the reference location (Δd) for Annecy (left), Aubenas (middle) and Karlsruhe (right). ρ and RMSD are calculated for $X\delta D_{pwf}$ time series starting at 00 UTC 13 June 2019 of different length: 24 h (orange), 48 h (blue), 72 h (magenta) and 120 h (black). The 5-95 percentile range is only shown for the 120 h time series.

For RMSD, the opposite dependency on Δd than for ρ can be seen (Fig. 6). For Annecy and Aubenas, there is a high spread in RMSD (see 5-95 percentile range) for 50 km and higher Δd. For Karlsruhe, RMSD and its spread increase continuously with distance until an equilibrium is reached at 500 km. The 120 h time window of the time series used for the analysis of the spatial scales does not allow to study the temporal evolution of the spatial scales. In Fig. 6, the mean Δd-ρ and Δd-RMSD relationship are shown for shorter time windows of 24 h, 48 h and 72 h with the same starting time as the 120h time series. The mean relationships for 48 h and 72 h are similar to the 120 h relationship for ρ and RMSD. Due to only a few data points in the 24 h time series, the Δd-ρ relationship is less stable than for the other time windows, whereas RMSD relationship is similar for all time windows. As a compromise between temporal resolution and the number of data points, a 48h time window will be studied in the following.

Additionally to the topography, the synoptic situation strongly impacts the spatial scales of $X\delta D_{pwf}$ features at a given location. This is shown for 48 h $X\delta D_{pwf}$ time series correlated with Annecy in Fig. 7. The locations with ρ > 0.8 and RMSD < 8 ‰ are shaded for different 48 h time windows in both

COSMO$_{iso}$ simulations. Depending on the start time, the area of $\rho > 0.8$ is either confined to an area within 50 km of the origin (see for example start time 20 June 00 UTC, red contour) or the area spreads over a large region north of the Alpine mountain range (see start time 18 June 00 UTC, yellow contour). In the time window from 00 UTC 18 June to 00 UTC 20 June, a low pressure system passes over Northern France and Germany (Fig. 8a,b), which influenced XδD$_{pwf}$ over a large region. The yellow region in Fig. 7 mainly resided in the warm sector of this low pressure system and experienced similar variability in XδD$_{pwf}$ within 48 h. This large area of correlation for Annecy on 18-20 June stays in contrast to a relatively small area of up to 100 km distance from the reference point of high correlation in Karlsruhe (not shown). Karlsruhe experienced faster changes in XδD$_{pwf}$ during this time due to its proximity to the cyclone center and flatter terrain leading to lower spatial scales of correlation. On 20-22 June, the pressure gradient is relatively weak over central Europe (Fig. 8c,d). Therefore, local convection and small-scale processes influence XδD$_{pwf}$. Due to the weak large-scale forcing, a high spatial variability in XδD$_{pwf}$ leads to a small region of high correlation around Annecy. At Karlsruhe, the region of high correlation covers an area of similar size for 20-22 June as for 18-20 June showing that the spatial scales at this site are less strongly influenced by the large-scale flow during the study period.

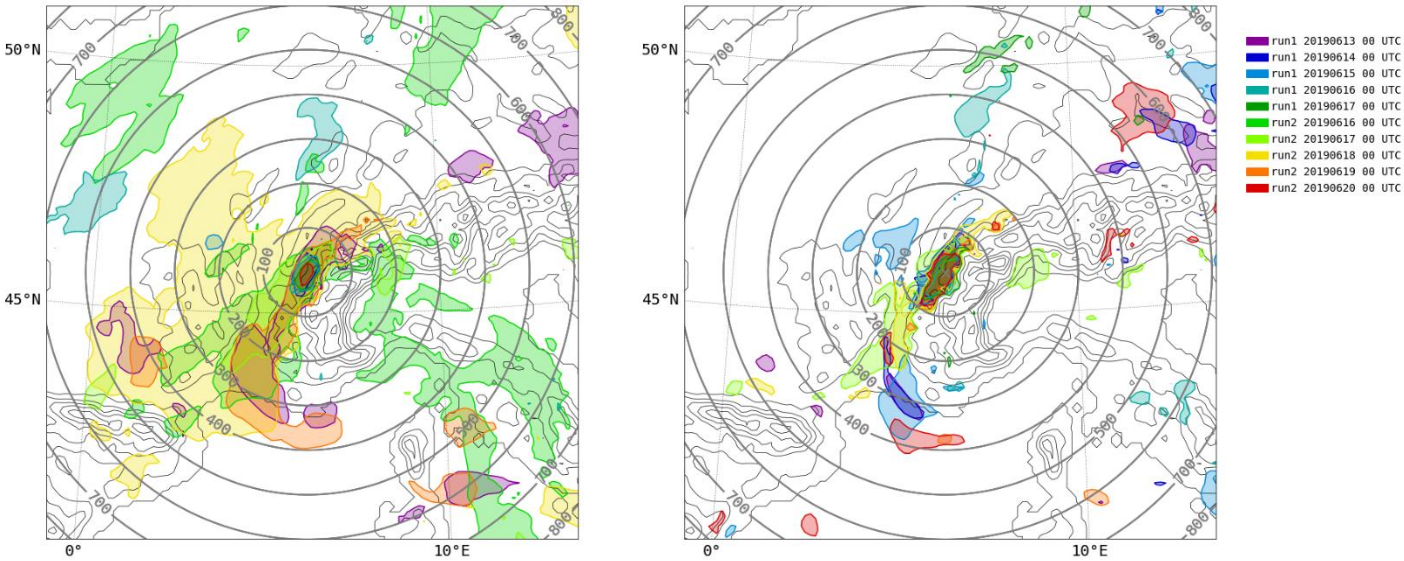

Figure 7: Maps showing the filled contours of regions with a Pearsons correlation coefficient of $\rho > 0.8$ (left) and RMSD < 8 ‰ (right) for 48h time series starting between 00 UTC on 13 June and 00 UTC on 20 June (colors) of XδD$_{pwf}$ at Annecy and any other points in the COSMO$_{iso}$ domain. The grey circles show distance from the reference location in 100 km steps and the black contour the topography.

In contrast to ρ, RMSD covers a similar area north of the Alps for most time windows with the largest overlap in an region within 100 km from the reference point (Fig. 7). These similar areas of RMSD < 8 ‰ during the campaign indicate that these regions to the northwest of the Alps show generally similar absolute values of XδD$_{pwf}$. The more variable regions of high ρ show the high temporal XδD$_{pwf}$ variability, which strongly influence the correlation of XδD$_{pwf}$ time series at different locations. To define the representative spatial scales for $X\delta D_{pwf}$ at a given location such as Annecy, the ρ and RMSD metrics as shown in Fig. 7 can be combined in various ways, depending on the goals of the analysis. High correlation regions connect areas of similar temporal variability, but not necessarily similar absolute values. Low RMSD regions represent areas of similar absolute values, but do include information on the short-scale variability. For the combination of the two metrics, a restrictive method is to only include pixels for which the correlation is high and RMSD low. Using this method, all selected pixels represent areas of similar temporal evolution and a small off-set in isotopic composition. For satellite data, which are masked by cloud coverage, this restrictive method can lead to too small sample sizes. A less restrictive method is to include all points, which have either a high correlation or low RMSD with the reference location. The selected pixels of this method represent regions with an isotopic composition related to the reference location either by temporal variability or similar absolute values. As shown in Fig. 9, for most time steps the best mask to exclude clearly different air masses from the reference location, but still include enough pixels, is a combination of both metrics by meeting either criteria for each pixel. For the L-WAIVE campaign period, a combined mask using $\rho > 0.8$ and RMSD < 8 ‰ and a distance of less than 400 km from the L-WAIVE campaign site has been found to well represent the spatial scales of XδD at Annecy. For 17 June, a 100 km instead of 400 km distance mask is needed to well represent XδD at Annecy (Fig. 9) due to very strong XδD-gradients within 400 km distance (see Appendix figure A2). A time-dependent mask based on 48 h time series of $X\delta D_{pwd}$ will be used for the comparison of the datasets in the next section using the criteria $\rho > 0.8$ and RMSD < 8 ‰.

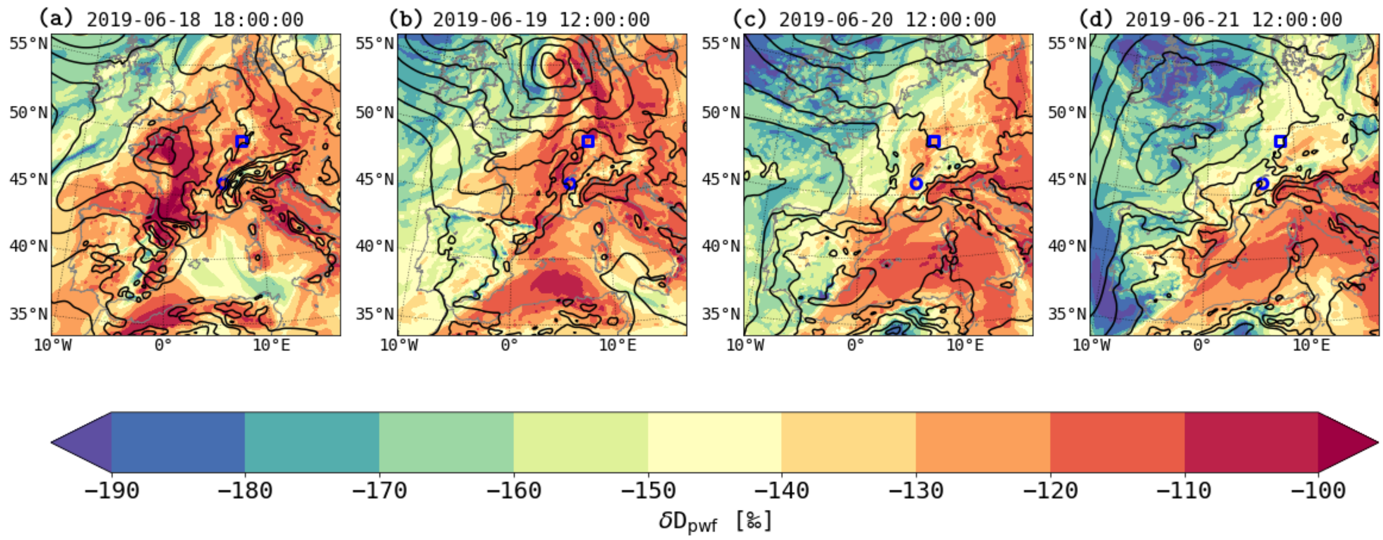

Figure 8: $X\delta D_{pwf}$ (colors) and sea level pressure (black contours) in CI_{15} at (a) 18 UTC 18 June 2019, (b) 12 UTC 19 June 2019, (c) 12 UTC 20 June 2019 and (d) 12 UTC 21 June 2019. The blue circle denotes the location of Annecy, the blue square Karlsruhe.

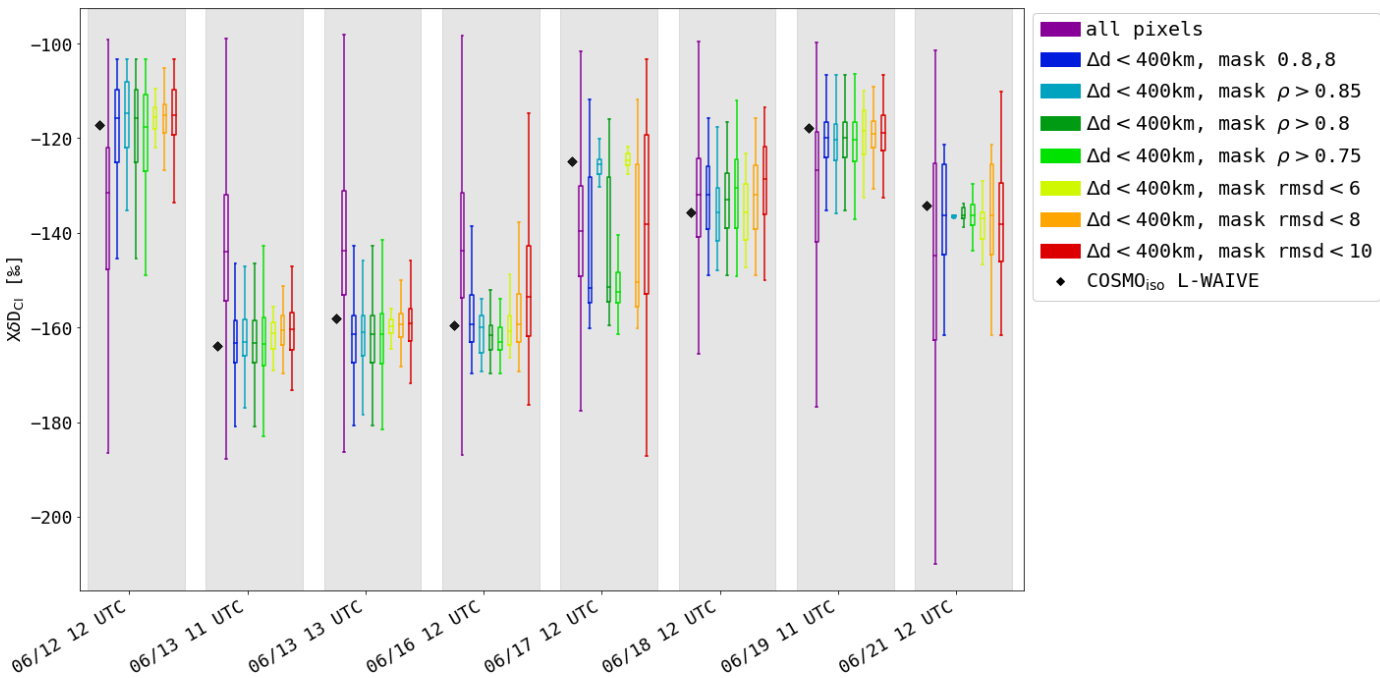

Figure 9: Boxplots of XδD in $COSMO_{iso}$ simulations for time steps with collocated satellite overpasses and different pixel selection criteria: all pixels (violet), pixels less than 400 km from Annecy and a combined mask of ρ > 0.8 and RMSD < 8 ‰ (blue), ρ > 0.85 (light blue), ρ > 0.8 (dark green), ρ > 0.75 (light green), RMSD < 6 ‰ (yellow), RMSD < 8 ‰ (orange) and RMSD < 10 ‰ (red). The interpolated XδD in $COSMO_{iso}$ at Annecy is shown as a black dot for each time step.

6.1.2 Comparison of datasets

In the previous section, we derived an instrumentation to compare and combine datasets of different spatial and temporal resolution. There are different levels of pre-selection of the compared data points. Based on the minimum length scale of correlation for a specific location, a radius can be defined to select only points closer to the location to be compared with the measured values. To account for the dynamic and often asymmetric nature of the high correlation regions, we use a mask to select data points located in a region based on e.g. a threshold of ρ. Further, specific criteria based on the retrieval properties need to be applied. For a meaningful comparison of total or sub column δD, the surface pressure in the retrieval and simulated or measured at the measurement site should agree closely. Therefore, a threshold is used to exclude pixels with a large difference in surface pressure between the retrieval and the simulation or measurement.

In the following, the total column S5P retrieval are compared to simulated COSMOiso XδDpwf for the L-WAIVE location to evaluate the performance of different masks based on the studied spatial scales. As an outlook, subcolumn S5P retrievals are compared to pseudo retrievals based on the in - situ δD profiles illustrating how a comparison of subcolumns can be approached.

6.1.2.1 COSMOiso simulations and S5P total column retrievals

For this comparison between model and satellite data, the $COSMO_{iso}$ pseudo total column values based on the pressure weighting function as described in Sec. 5.1 are used together with S5P-TROPOMI L2 product v1.0. For the simulation time period from 12 to 22 June 2019, satellite overpasses over the model domain are identified and filtered for a quality value of 2. A satellite overpass is considered to be collocated with the COSMOiso simulation if the overpass shows any quality filtered pixels within the $COSMO_{iso}$ domain. For each satellite pixel, the $COSMO_{iso}$ total column values are interpolated. Further, only pixels are selected for which the pressure difference between the surface pressure of the retrieval and in the $COSMO_{iso}$ simulation is less than 10 hPa. Fig. 10 shows the difference between the $COSMO_{iso}$ and L2 product XδD for selected collocated satellite overpasses. The mean difference is 25.8 ‰ with a [25,75]-percentile range of 4.5- 50.1 ‰ and highly variable depending on time and location. Many overpasses over the Iberian peninsula and the Pyrenees show a positive bias. Smaller differences are often seen over Eastern Europe. Fig. 11 shows the distributions of the difference between $COSMO_{iso}$ and S5P for XδD and total column mixing ratio (r) binned for longitude, latitude and altitude. $COSMO_{iso}$ r is mostly drier than S5P. There is no clear trend in humidity difference with latitude, longitude or altitude, except for a decrease in the difference in δD with longitude. Most pixels for altitudes above 1500 m a.s.l. are filtered out due to a surface pressure difference above 10 hPa between $COSMO_{iso}$ and S5P. This pressure difference could be due to differences in the representation of the complex topography of high-altitude regions in the $COSMO_{iso}$ simulations and the retrieval model. To avoid the filtering of pixels above 1500 m a.s.l. more detailed investigations of the topography and pixel sizes are needed. For a higher confidence in $COSMO_{iso}$'s performance at high altitudes, higher resolution simulations (e.g. 0.02°) should be conducted in future studies. Further, the $COSMO_{iso}$ vertical water vapour profiles could be extrapolated or truncated to correspond to the retrieval profiles' vertical extent. For such an extrapolation of vertical isotope profiles over high altitude regions, further analyses (preferably including measurements of vertical δD variability and higher resolution $COSMO_{iso}$ simulations) are needed to understand the vertical variability of $COSMO_{iso}$ over these regions.

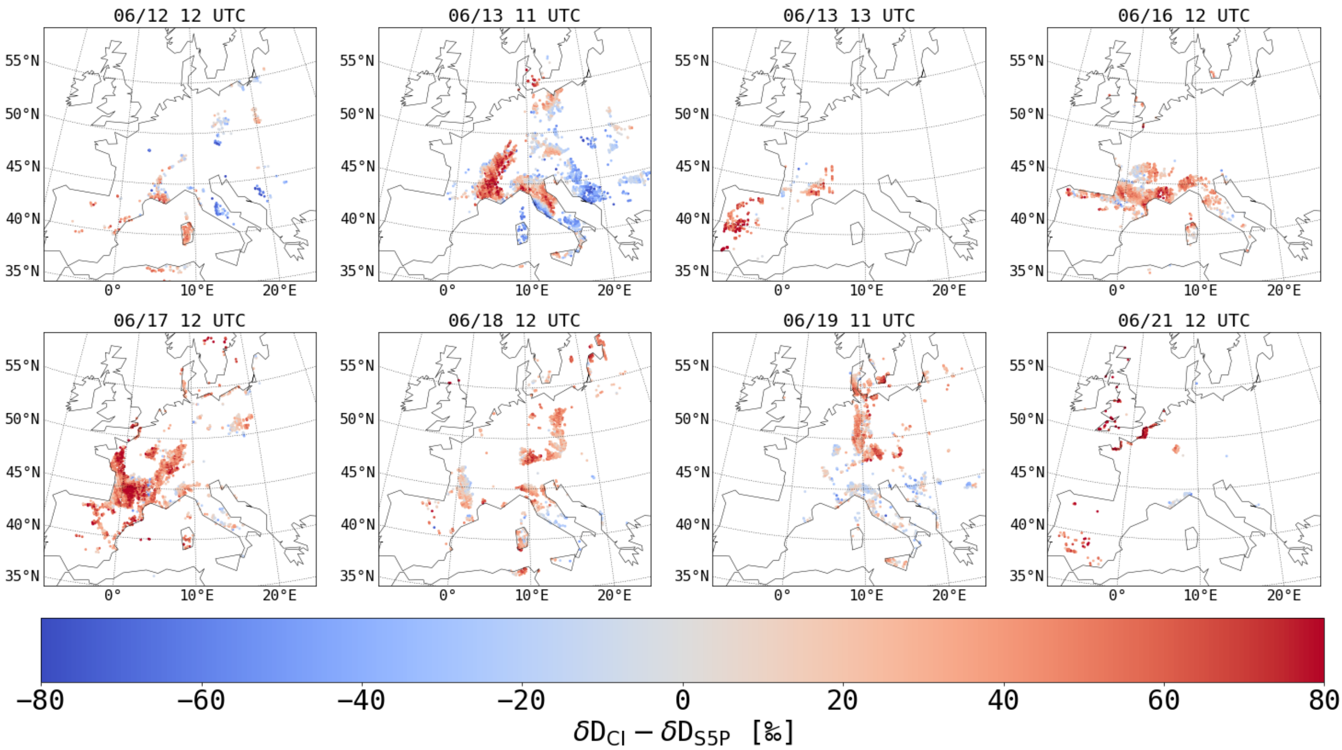

Figure 10: Difference between total column δD from COSMO$_{iso}$ simulations and S5P retrievals for selected collocated satellite overpasses. For all collocations see Appendix Figure A1.

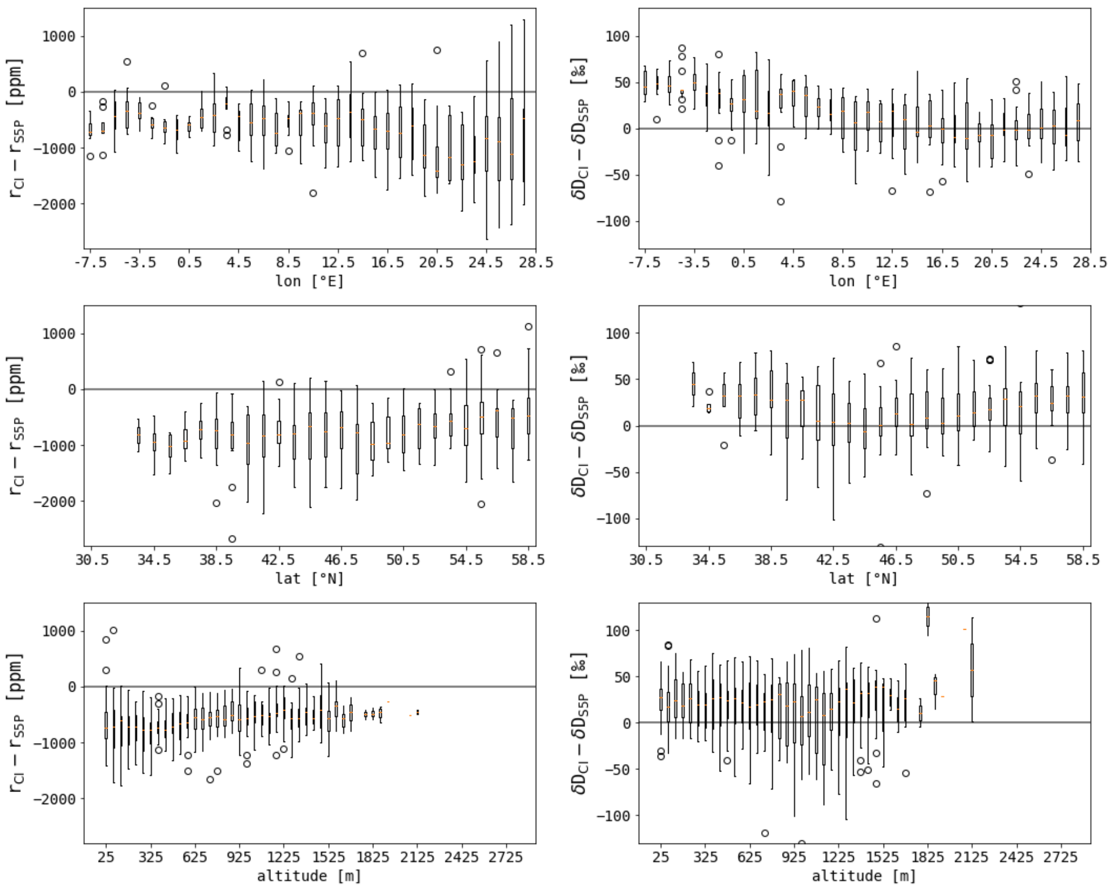

Figure 11: Boxplots of the difference between COSMO$_{iso}$ simulations and S5P retrievals in total column water mixing ratio (r, left) and δD (right) binned for longitude (top), latitude (middle) and altitude (bottom).

To test different levels of pre-selection criteria of pixels for the comparison of point measurements with satellite overpasses, distributions of XδD for different regions around the location of the L-WAIVE campaign are shown in Fig. 12 using COSMO$_{iso}$ and S5P total column data. At the L-WAIVE location, COSMO$_{iso}$ shows higher values than collocated satellite overpasses (Fig. 12, black diamond). The largest change in the XδD distribution of the selected pixels in COSMO$_{iso}$ appears when applying the weakest criteria of a distance of less than 400 km from the measurement site (blue boxplots in Fig. 12). Depending on the XδD variability within the 400 km radius, applying a stronger criterium of a mask based on the $\rho > 0.8$ and RMSD < 8 ‰ contours in the two simulations leads to a narrower distribution and a mean δD very close to the COSMO$_{iso}$ value at the measurement Location (see e.g. 11 UTC on 13 June in Fig. 12). For the S5P data, the variability due to different selection criteria is larger than for COSMO$_{iso}$. This is due to higher XδD variability of in the satellite retrievals than in COSMO$_{iso}$. In contrast to COSMO$_{iso}$, the application of a pre-selection criterium shows that the computed mean value of the S5P retrievals can be strongly modified due to changes in the radius of the region or applying an additional mask. An explanation of this difference in variability could be that the spatial scales derived from $COSMO_{iso}$ simulations overestimate the size of the correlation area due to too low spatial variability in δD. An increased spatial resolution of $COSMO_{iso}$ simulations might lead to more variable δD in the Alpine region due to a better representation of convective processes. Further, the satellite retrievals show relatively low XδD compared to $COSMO_{iso}$. Instead of using only pressure weighting functions for the $COSMO_{iso}$ total column values, the kernel from the S5P retrieval could also be applied to the $COSMO_{iso}$ dataset. Including the apriori profiles in the calculations of the $COSMO_{iso}$ profiles might decrease some of the current differences between the datasets.

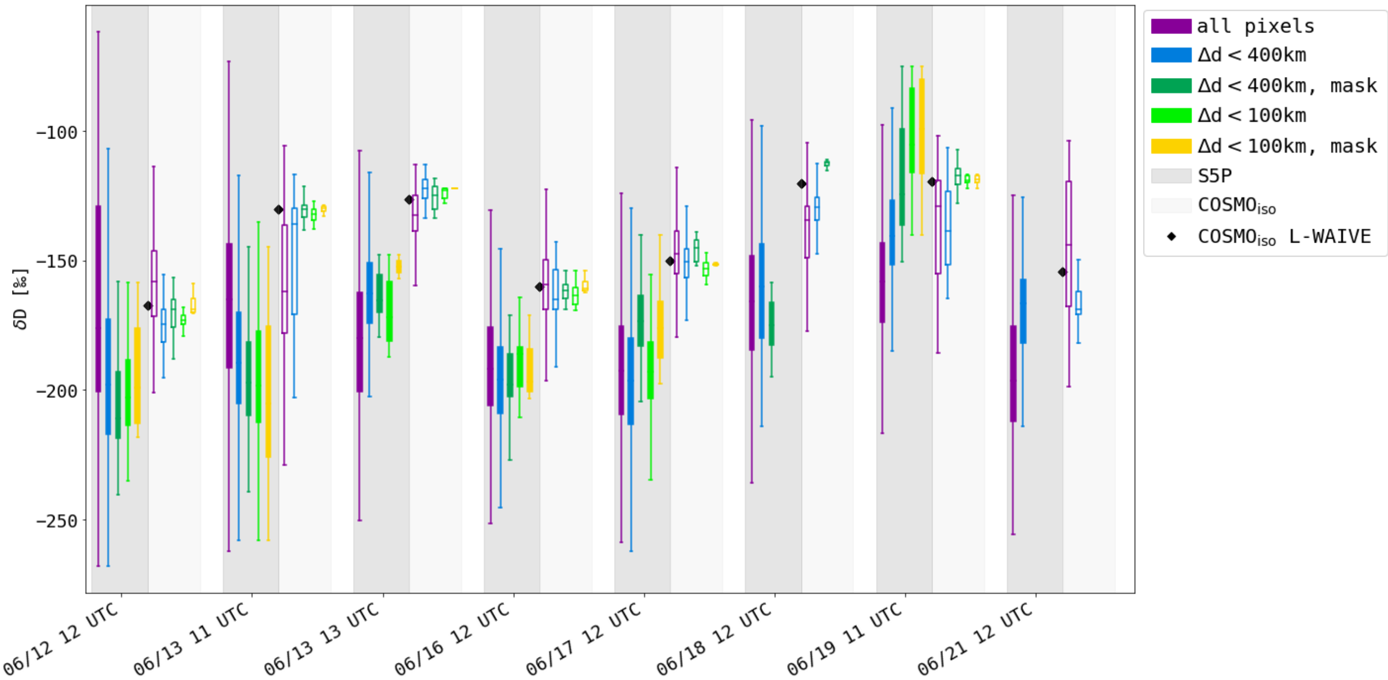

Figure 12: Boxplots of total column δD in S5P retrievals (dark grey background, filled boxplots) and $COSMO_{iso}$ simulations (light grey background, empty boxplots) for collocated satellite overpasses and different pixel selection criteria: all pixels (violet), Δd < 400km (blue), Δd < 400km and mask based on ρ > 0.8 and RMSD < 8 ‰ (dark green), Δd < 100km (light green) and Δd < 100km and mask based on ρ > 0.8 and RMSD < 8 ‰ (yellow). The interpolated total column δD from $COSMO_{iso}$ in Annecy is shown as a black dot for each satellite overpass. Pixels with more than 10 hPa difference in surface pressure between the retrieval and the simulations are excluded.

6.1.2.2 L-WAIVE and S5P subcolumn retrievals

The in-situ vertical δD profiles from the L-WAIVE campaign reach an altitude of maximum 3500 m. To compare these subcolumn profiles to the satellite retrievals, the profiles can be (i) extrapolated using assumptions on the vertical δD distribution above 3500 m, or (ii) be compared to S5P subcolumn retrievals, which only cover the corresponding altitudes of the in-situ measurements. Here, we show preliminary results using the option (ii) of a comparison of subcolumn retrievals from the S5P-TROPOMI data (see Sec. 5.1) and pseudo subcolumn values based on the measured profiles during the L-WAIVE-campaign (see Sec. 5.2).

Figure 13 shows the difference between the S5P and L-WAIVE subcolumn values for each flight in comparison with the satellite overpass which is closest in time. For four of the overpasses, the subcolumns based on the L-WAIVE profiles show higher δD than the satellite subcolumn retrievals. For the last satellite overpass on 19 June, the satellite retrievals show values around -50‰, which are relatively high for δD in atmospheric water vapour as they lie above the value expected from ocean evaporation. Further investigation is needed to see where these unrealistic values originate. Simultaneously, the in-situ measurements on 19 June were partly affected by high humidity in the inlet line. Therefore, some caution is used during the interpretation of this last overpass.

The impact of different pixel selection criteria on the distribution of δD around the L-WAIVE location varies depending on the day and the dataset (Fig. 14). For 13, 14, 16 and 17 June, the spread of the distribution changes similarly for the L-WAIVE and S5P subcolumns. Further, the distributions are narrower if the mask is applied, but not necessarily if the distance from the measurement site is decrease (see e.g. 13 and 17 June). This indicates that the mask serves as a good tool to choose pixels of the same air mass. For these four days, the satellite coverage is relatively good with many pixels close to the measurement site. On 18 to 20 June, there are less pixels close to Annecy and, therefore, the distributions are more sensitive to different selection criteria than for the days before.

Several further investigations are needed to better understand the differences seen in subcolumn δD from S5P and L-WAIVE. Further retrieval parameters, such as the degrees of freedom and total column water vapour, should be analysed to pinpoint the factors leading to unrealistic high δD subcolumn retrievals on 19 June. Using the total column water vapour, paired distribution with δD can be compared for L-WAIVE and S5P subcolumns. To increase the number of collocated points during a satellite overpass, the in-situ profiles could be extrapolated to the surface to account for surface pressure differences. Furthermore, extending this analysis to further locations, such as Aubenas, and high-resolution $COSMO_{iso}$ simulations would indicate how strongly the local topography around Annecy affects the spatial representativeness of the measurements.

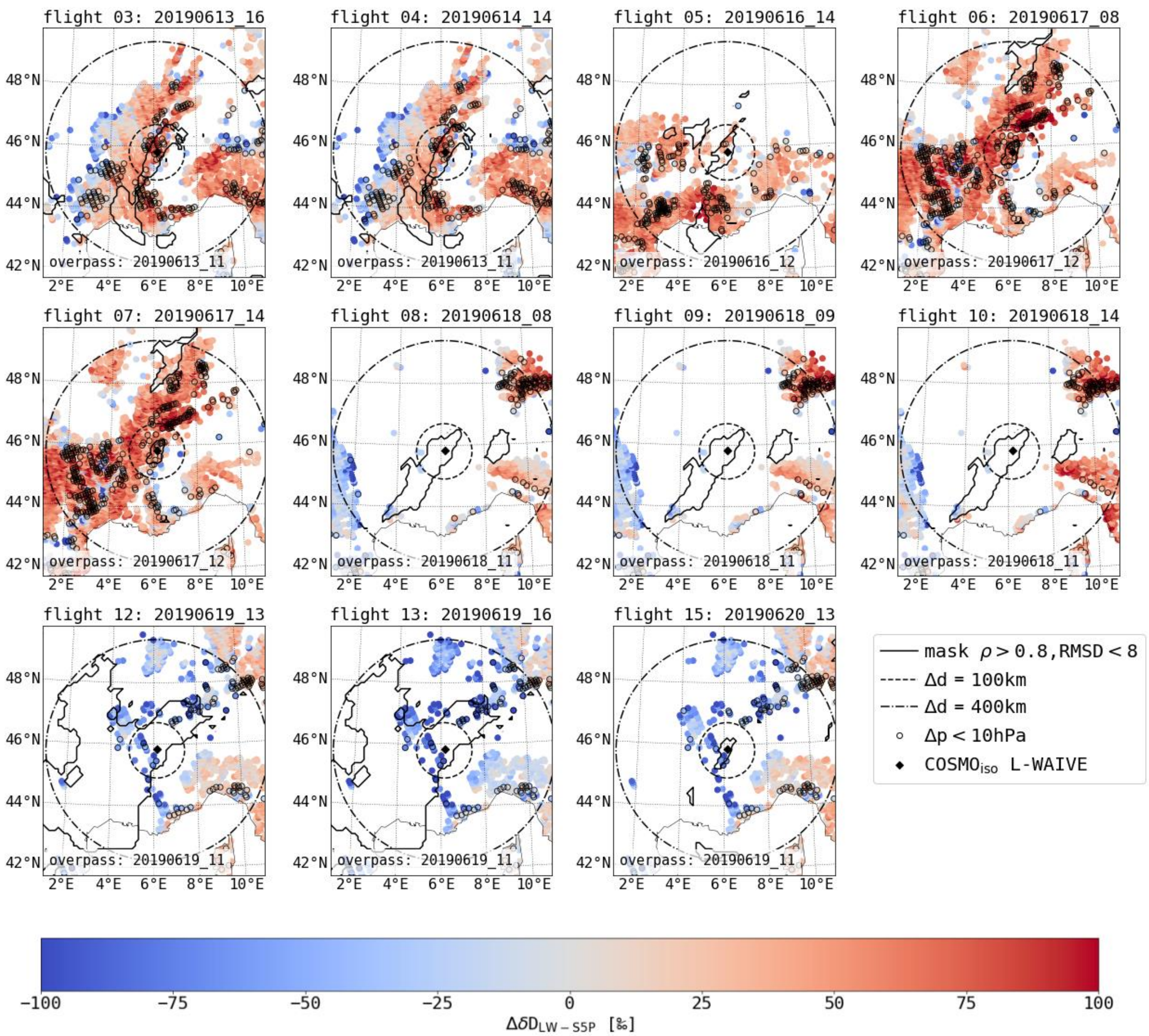

Figure 13: Scatterplots of the difference between S5P subcolumn retrievals and L-WAIVE subcolumns (colours). The black dashed circles show Δd = 100 km and Δd = 400 km. The black solid lines show the mask based on ρ > 0.8 and RMSD < 8 ‰. The black framed markers mark pixels with less than 10 hPa difference in surface pressure between the retrieval and the pressure at the lowermost point of the in situ profiles. The date in the title is the time of the in situ profile, the date in the lower left corner is the time of the satellite overpass. The black diamond is the location of the measurements during the L-WAIVE campaign.

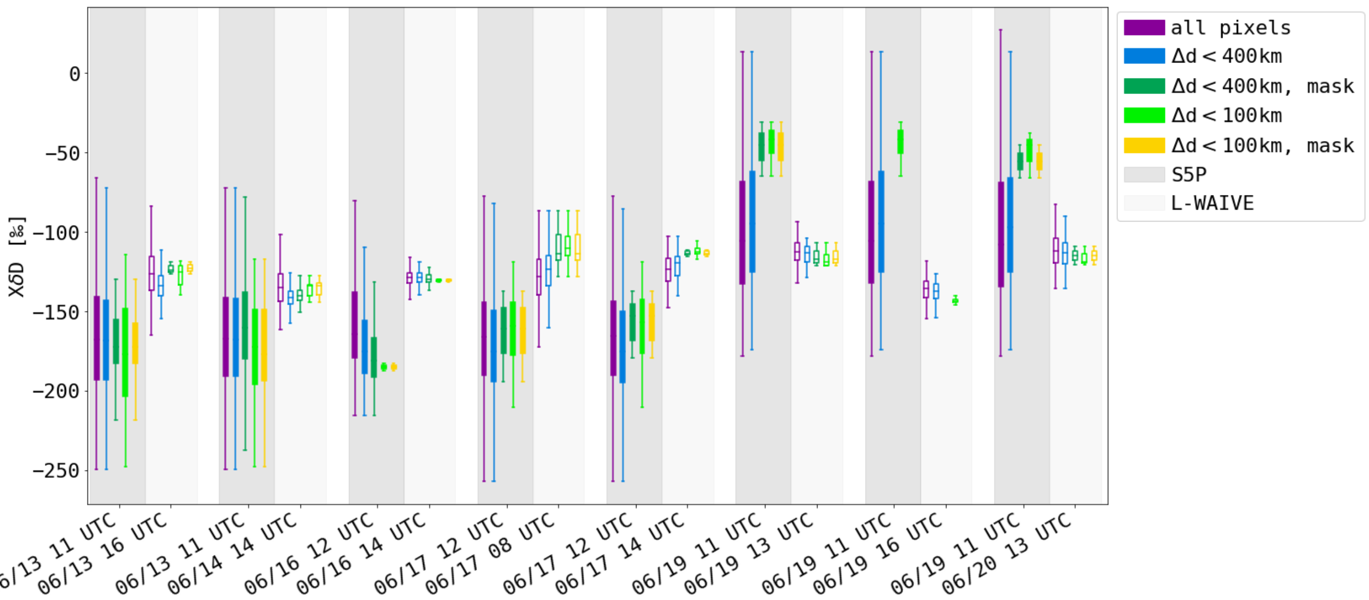

Figure 14: Boxplots of subcolumn δD in S5P retrievals (dark grey background, filled boxplots) and using the L-WAIVE measurements (light grey background, empty boxplots) for collocated satellite overpasses and different pixel selection criteria: all pixels (violet), $\Delta d < 400$ km (blue), $\Delta d < 400$ km and mask based on $\rho > 0.8$ and RMSD < 8 ‰ (dark green), $\Delta d < 100$ km (light green) and $\Delta d < 100$ km and mask based on $\rho > 0.8$ and RMSD < 8 ‰ (yellow). Only pixels with less than 10 hPa difference in surface pressure between the retrieval and the pressure at the lowermost point of the in situ profiles are included.

6.2 Analysis of {H_2O, δD} pair distributions over the Sahel region

As motivated in [AR 1], the hydrological cycle over West Africa is marked by highly varying conditions, from extremely dry winter months to very intense convective rainfalls during the summer months (see Fig. 15). While the former is a period with strong trade winds carrying dry air masses from the Sahara into the Sahel, the latter is associated with the so-called West African Monsoon, which leads, through complex interactions between large-scale dynamical and small-scale microphysical processes, to convective rainfall events over the Sahel from June to September. In total, the monsoon rainfalls account to more than 80% of the annual Sahelian rainfall (Dhonneur, 1981; Fink et al., 2006). As suggested by Fig. 15, the complexity of these rainfall pattern require a certain sophistication of the model. The model agrees best with the observation of GPM IMERG (Huffman et al., 2019) the better the horizontal resolution and the more sophisticated the different scales are connected (two way nesting between the global scale (coarse resolution) and the local scale (high resolution)).

The phenomenon of strongly increased precipitation during the monsoon period is mainly driven by the northward shift of the sun zenith, which shifts the zonal belt of tropical convection from the eastern Tropical Atlantic towards the West African coast. Thermal effects and dynamical feedbacks lead then to an abrupt jump of maximum precipitation from the Guinean Coast (see difference in the IMERG precipitation patterns between November-May and August in Fig. 15) to the semi-arid Sahel zone up to 15-20° N (Sultan and Janicot, 2003). During this period, south-easterly winds intensify and transport moisture from the Tropical Atlantic into the Sahel, where they are opposed to the dry north-westerly trade winds from the Sahara. Figure 16 reveals the typical wind fields at 625 and 925 hPa over the Sahel and demonstrates that there can be tremendous differences in where the air comes from for the boundary layer (925 hPa) and the mid-troposphere (625 hPa). The air masses in the mid-troposphere show large contributions from large-scale transport, e.g. from the upper troposphere (e.g. the African Easterly Jet, see subsiding trajectories in the upper panel of Fig. 16) or from Northern Africa (anticyclonic rising air mass transport in upper panel of Fig. 16). In contrast, the boundary layer is marked by rather local dynamical effects, e.g. the near-surface south-easterly monsoon winds from the Tropical Atlantic (see rising trajectories in the lower panel of Fig. 16).

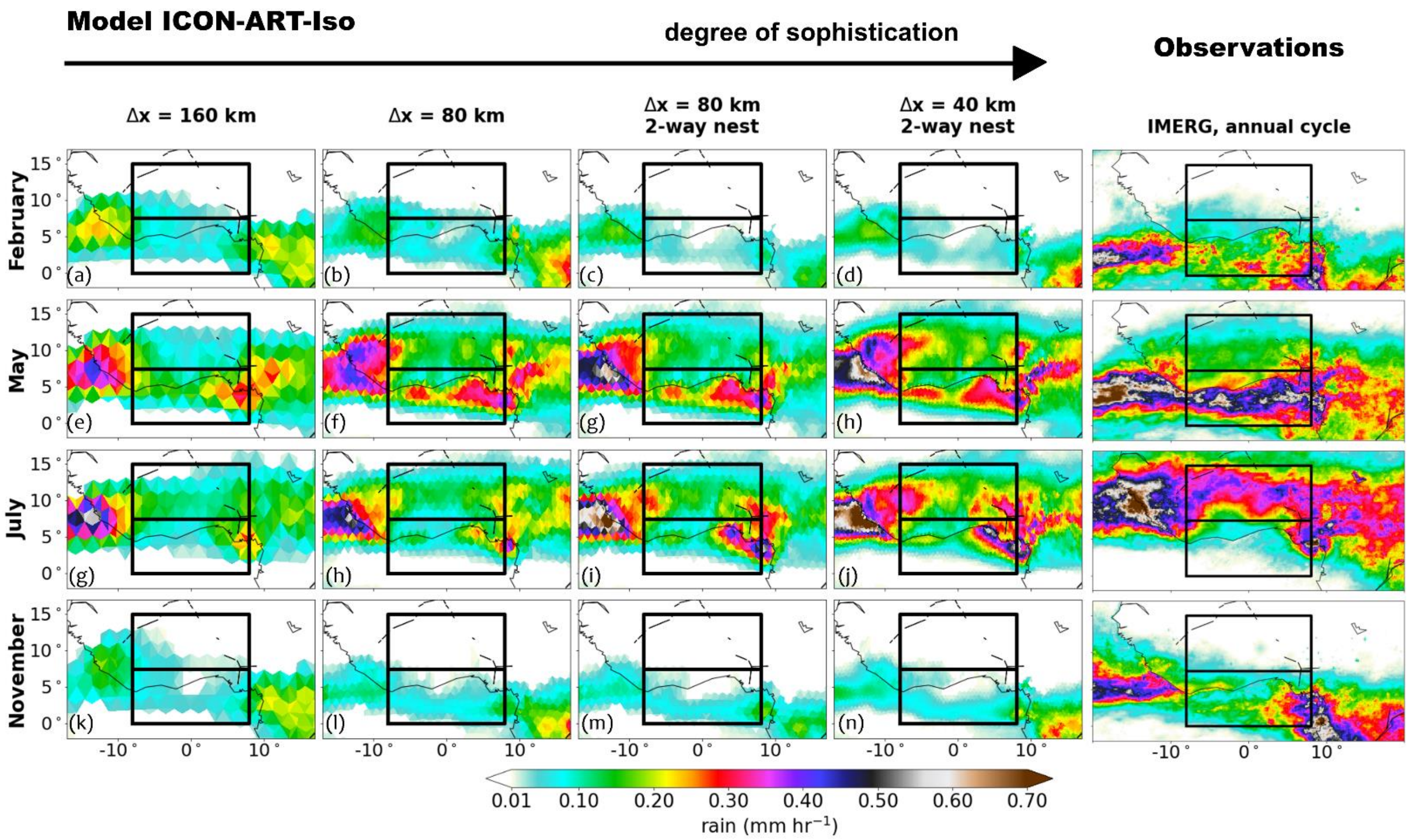

Figure 15: Monthly averages of hourly precipitation over West Africa as simulated by ICON-ART-Iso using different degrees of model sophistication and as provided by GPM IMERG (Huffman et al., 2019). The black box marks the area over the Sahel and the Guinea Coast.

However, as water vapour strongly depends on the prevailing wind fields, this heterogeneity also affects tropospheric water vapour profiles. For instance, the mid-tropospheric water vapour content strongly depends on the moisture signals from large-scale air mass transport with additional contributions from local and high-reaching convection, while in the boundary layer local surface evaporation might be an important moisture source.

The following sections will assess how the S5P data may support the analysis of water vapour variability during the West African Monsoon and how they may provide supplementary information to already existing water isotope data, here from MUSICA IASI (Sect. 5.3). For this purpose, we will investigate additional model data from COSMOiso (Sect. 5.4.2) and ICON-ART-Iso (Sect. 5.4.3) and thereby focus on following three target altitude regions:

- Mid-troposphere around 600 hPa, which represents the layer of main sensitivity of the MUSICA IASI {H_2O, δD} pair product (Schneider et al., 2016; Schneider et al., 2021a; Diekmann et al., 2021b).

- Total columns of H_2O and δD to represent the characteristics of the S5P data product.
- Boundary layer around 900 hPa, where increased sensitivity is expected for a potential water vapour isotope product generated by combing MUSICA IASI and S5P data.

In order to interpret the observed and modelled {H_2O, δD} pair distributions with respect to the underlying dynamical and microphysical processes, we make use of a theoretical interpretative framework from Diekmann et al. (2021a), which uses idealized process curves to attribute characteristic variations in paired distributions of H_2O and δD to underlying processes (see Fig. 17). These process curves mainly distinguish between characteristic {H_2O, δD} signals due to air mass mixing (hyperbolic curves, Fig. 17a), due to rain condensation (diagonal Rayleigh lines, shown in green in Fig. 17b) and due to rain evaporation in addition to rain condensation (Super-Rayleigh regime below the diagonal Rayleigh line, marked by the magenta Super-Rayleigh lines in Fig. 17b).

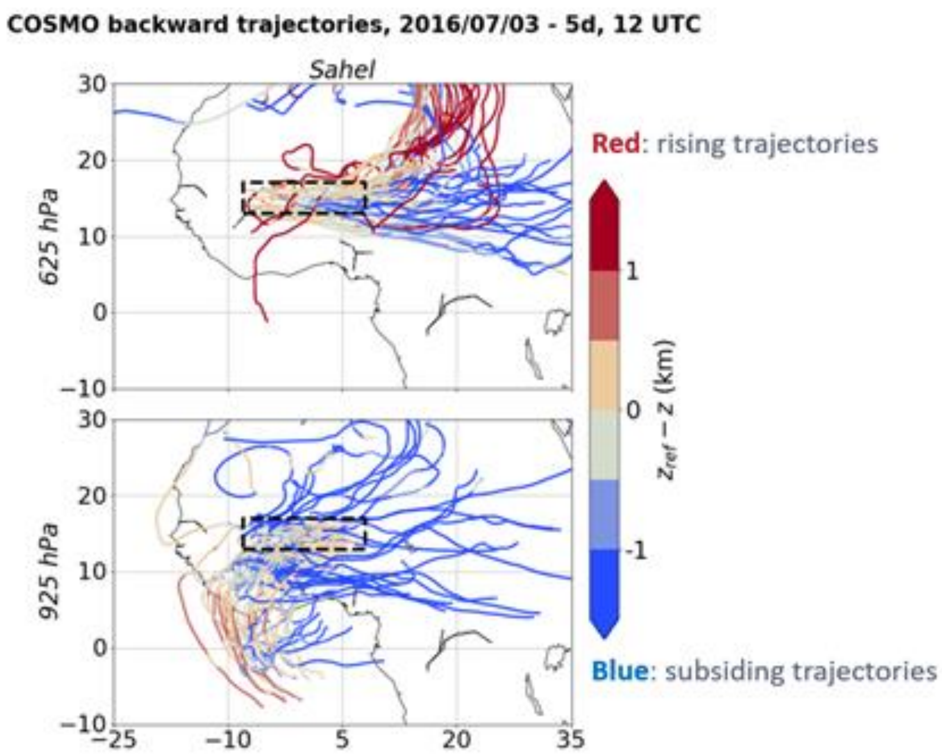

Figure 16: Backward air mass trajectories based on COSMO$_{iso}$ data over West Africa. Details about the trajectories are given in Diekmann et al. (2021b).

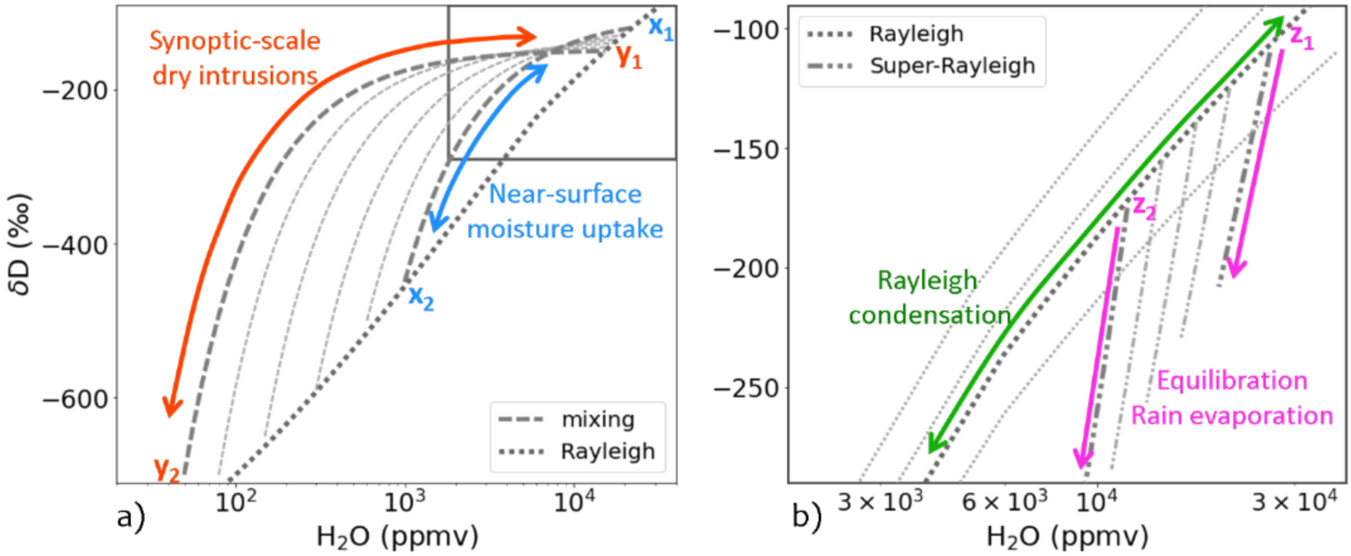

Figure 17: Theoretical curves as interpretative framework for {H_2O, δD} signals. (a) hyperbolic curves for describing characterizing effects due to air mass mixing. (b) diagonal lines for describing idealized signals due to Rayleigh condensation. The steeper Rayleigh lines describe idealized signals due to so-called Super-Rayleigh processes (rain evaporation in addition to rain condensation). An extensive discussion for these lines is given in Diekmann et al. (2021a).

6.2.1 Annual cycle

In a first step, data from the ICON-ART-Iso simulation (Sect. 5.4.3) are used to characterize the mean annual variability of {H_2O, δD} data within the Sahelian troposphere. This is done for the aforementioned target altitude regions: mid-troposphere (~640 hPa), boundary layer (~900 hPa) and the total column (see Fig. 18).

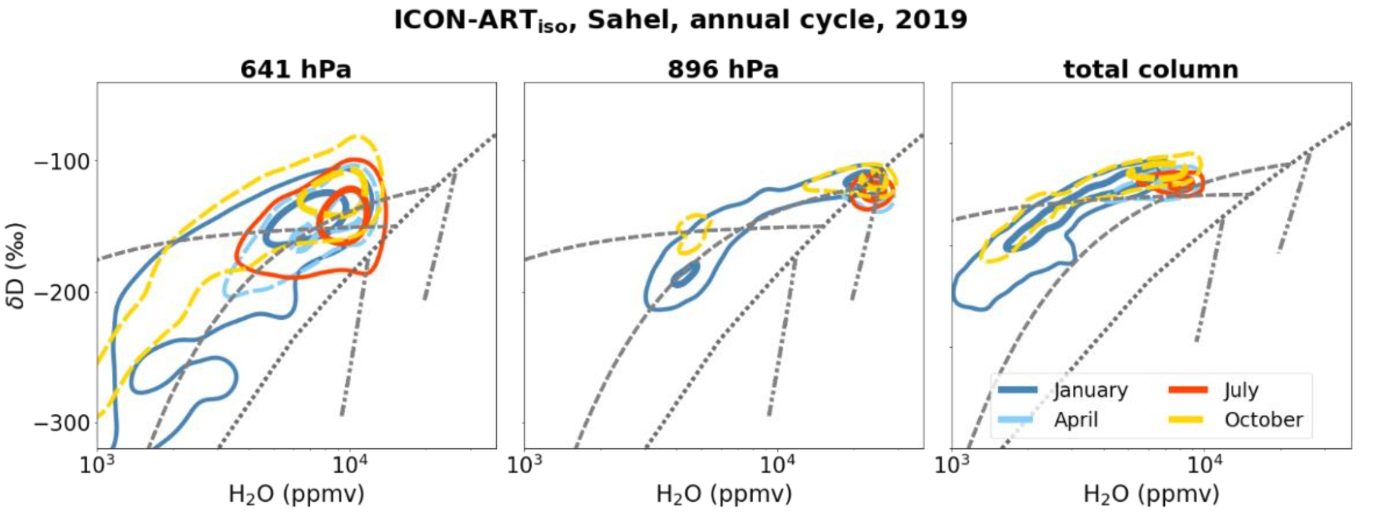

Figure 18: ICON-ART-Iso simulation of the annual cycle of the {H_2O,δD} distribution for the nested regions over the Sahel. The data of each month are described by two-dimensional frequency contours, with summarizing 50% and 95% of all respective data (calculation of contours according to Eckstein et al., 2018).

For all three target altitude regions, a large variability arises throughout the transition from winter to summer. During winter, the {H_2O, δD} distributions follow clearly the theoretical hyperbolic mixing curves, indicating strong contribution from air mass mixing. This is in agreement with the fact that during winter the northerly trade winds prevail, which mix dry air from the Sahara into the Sahel and thereby lead to relatively low values in H_2O and δD. In contrast, the monsoon system induces relatively high values in H_2O and δD at all target layers. In particular in the mid-troposphere, the {H_2O, δD} distribution shows an additional push towards the Rayleigh lines, which display the characteristic isotopic response to rain condensation, and even to the steeper Super-Rayleigh lines, which indicate the signals as response to evaporating rain (Fig. 17).

In a qualitative sense, this inter-annual variability can be seen in all target layers, even though in different regimes of the {H_2O, δD} phase space. However, it becomes apparent that the total column partially reflects the quantitative and qualitative structure of the boundary layer with an offset towards lower H_2O values, with still differences appearing in particular during October, where the total column rather reflects the structure of the mid-tropospheric signals. This makes clear that on an annual perspective the total column contains information from both layers (boundary layer and mid-troposphere).

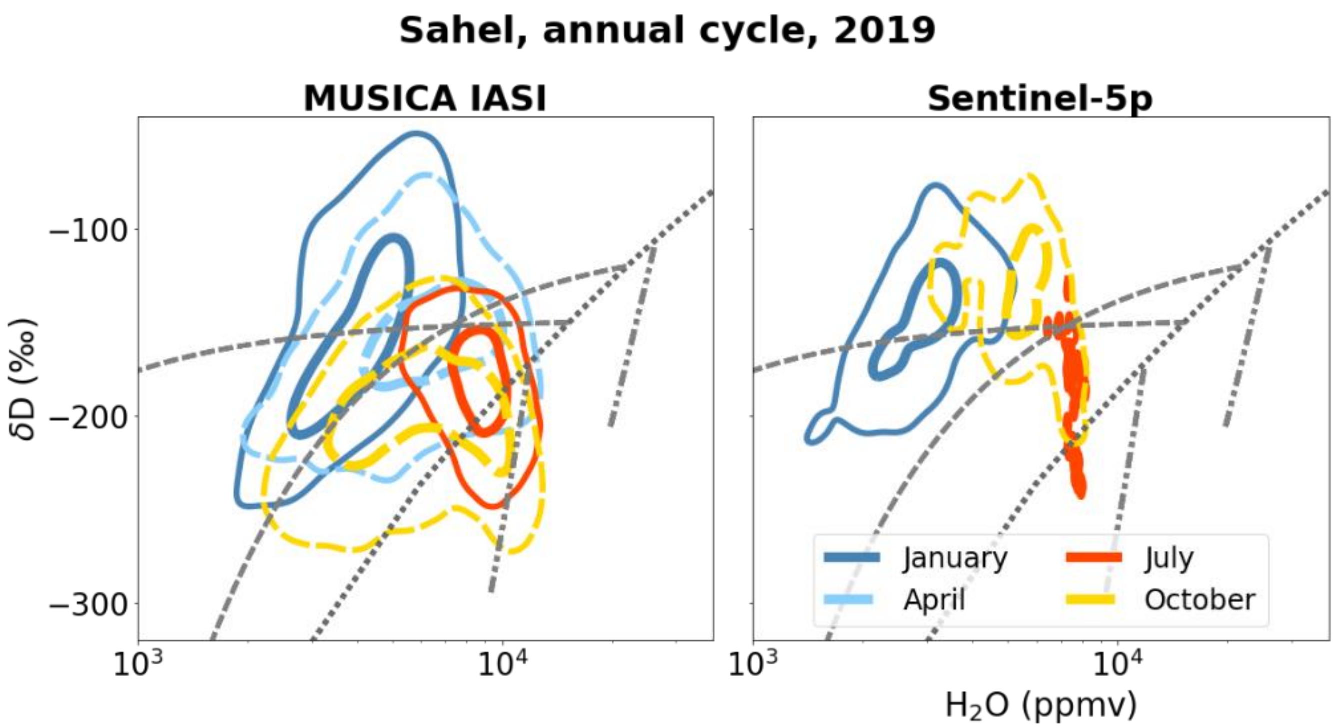

Figure 19: Data of MUSICA IASI and Sentinel-5P/TROPOMI showing the annual cycle of the {H_2O, δD} distribution over the Sahel.

In a next step, the annual cycle of {H_2O, δD} signals is investigated using the remote sensing products from MUSICA IASI and S5P (see Fig. 19). The comparison with Fig. 18 shows an overall reasonable agreement between the mid-tropospheric ICON-ART-Iso data and the MUSICA IASI data and between the total column data from ICON-ART-Iso and S5P, even though there are still some significant differences. For instance, ICON-ART-Iso shows largely drier values during winter in the mid-troposphere compared to IASI. This is due to the limited sensitivity of IASI at drier conditions (remote sensing data with low sensitivity are filtered out, whereas the model data in Fig. 18 are shown for all conditions). Furthermore, during summer the MUSICA IASI data show a very distinct anti-correlation between H_2O and δD, pushing the distribution strongly towards the steep Super-Rayleigh line. This phenomenon is a clear result of the increased microphysical rain processes during the monsoon precipitation, which is rather underestimated in ICON-ART-Iso. S5P also appears to reflect this transition from mixing signals during winter (similar to the total column of ICON-ART-Iso) to the summerly rain-induced anti-correlation between H_2O and δD. However, the application of the quality filtering of S5P (qa_value ≥ 1) removes almost all observations at that time and place.

6.2.2 Monsoon period (June to August 2018)

This section provides a more detailed view on the rainy season over West Africa, as the interaction between large-scale air mass transport and small-scale microphysical processes is most intense over the Sahel at this time. This allows to identify effects of convection and different water sources (with both remote ocean sources and local terrestrial sources), as done in detail in Diekmann et al. (2021a).

We use data from the COSMO$_{iso}$ simulation described in Sect. 5.4.2 to characterize the temporal evolution of {H_2O, δD} data over the Sahel for the period June to September 2018 (see Fig. 20). These COSMO$_{iso}$ simulations are made with a higher spatial resolution than the ICON-ART-Iso data used for the seasonal cycle study of the previous section (see the respective model setup descriptions in Sects 5.4.2 and 5.4.3). Analogous to Fig. 18, we distinguish between the three target altitude regions, i.e. the mid-troposphere, the boundary layer and the total column.

As response to the establishing monsoon conditions, especially in the mid-troposphere, a transition stands out from signals of large-scale air mass transport (June contours partly following the hyperbolic mixing line in left panel of Fig. 20) to increasing Rayleigh and Super-Rayleigh structures (push of contours towards lower δD values, left panel of Fig. 20). Following the discussions in Diekmann et al. (2021a), this is due to the depleting effect on δD caused by increased exchange between the condensed and the vapour phase within and close to convective systems.

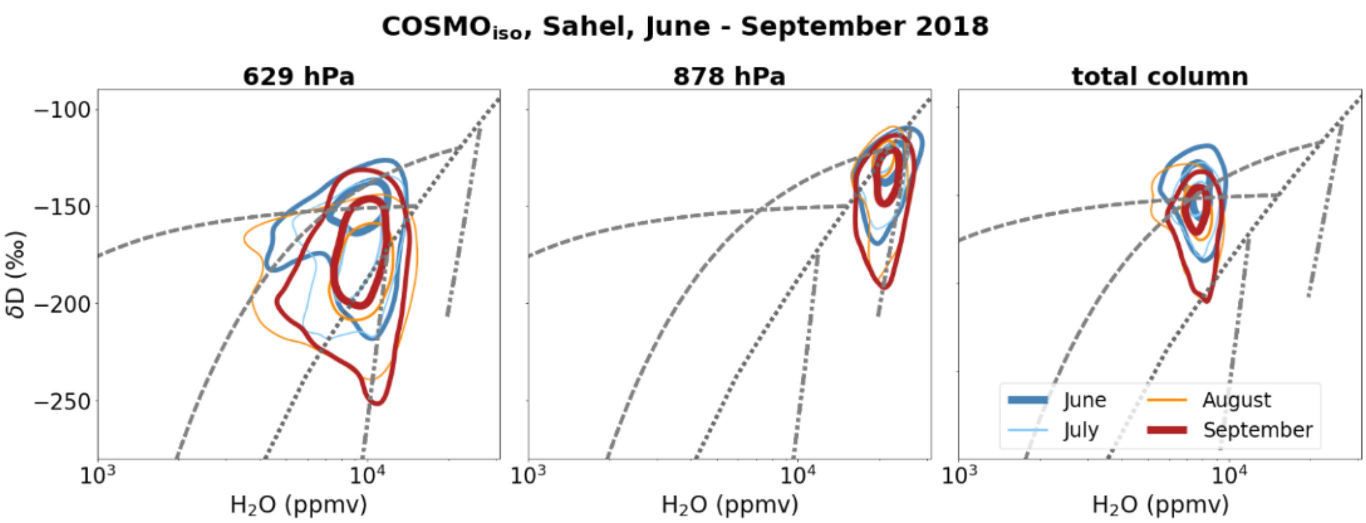

Figure 20: {H_2O, δD} data from COSMO$_{iso}$ (Sect. 5.4.2) over the Sahel during the Monsoon period in 2018. Two-dimensional contours summarize 50 and 95% of the corresponding data points. Additionally, the theoretical process curves from Diekmann et al. (2021a) are shown.

In the boundary layer, the mixing signals are less pronounced, as there rather local processes and evaporative sources determine the water vapour signals. This results in higher contents of H_2O and δD, however, with still a significant δD depletion towards the Super-Rayleigh regime (see middle panel in Fig. 20). Diekmann et al. (2021a) attributed the near-surface depletion in δD to sub-cloud rain evaporation in unsaturated downdrafts.

Similar to Fig. 18, the total column appears to reflect a mixture of signals from both the mid-troposphere and the boundary layer: the relative evolution of {H_2O, δD} from June to September agrees well with this from the boundary layer, with an offset to lower H_2O values towards the mid-tropospheric value range. The mid-tropospheric mixing signals are only faintly discernible in the total column, but the transition towards more depleted values for later months is clearly distinctive.

After determining the expected evolution of {H_2O, δD} along the rainy season over West Africa using model data, Fig. 21 shows the respective data from MUSICA IASI and S5P. In particular for MUSICA IASI, an overall high agreement to the mid-tropospheric structures modeled by $COSMO_{iso}$ is apparent: In the beginning of the rainy season (June), the {H_2O, δD} data show strong contributions from large-scale air mass mixing (following the hyperbolic mixing lines), whereas in the subsequent months the depletion towards the Super-Rayleigh regime increases as response to the increased rain interaction. Unfortunately, as also observed in the comparison with ICON-ART-Iso (Sect. 6.2.1), the current quality filtering of the S5P (qa_value ≥ 1) removes most S5P data over the Sahel during the summer months, what hampers a detailed evaluation of S5P data for this place and time. However, the few remaining data suggest a good agreement with the total column signals seen in the $COSMO_{iso}$ simulation (Fig. 20).

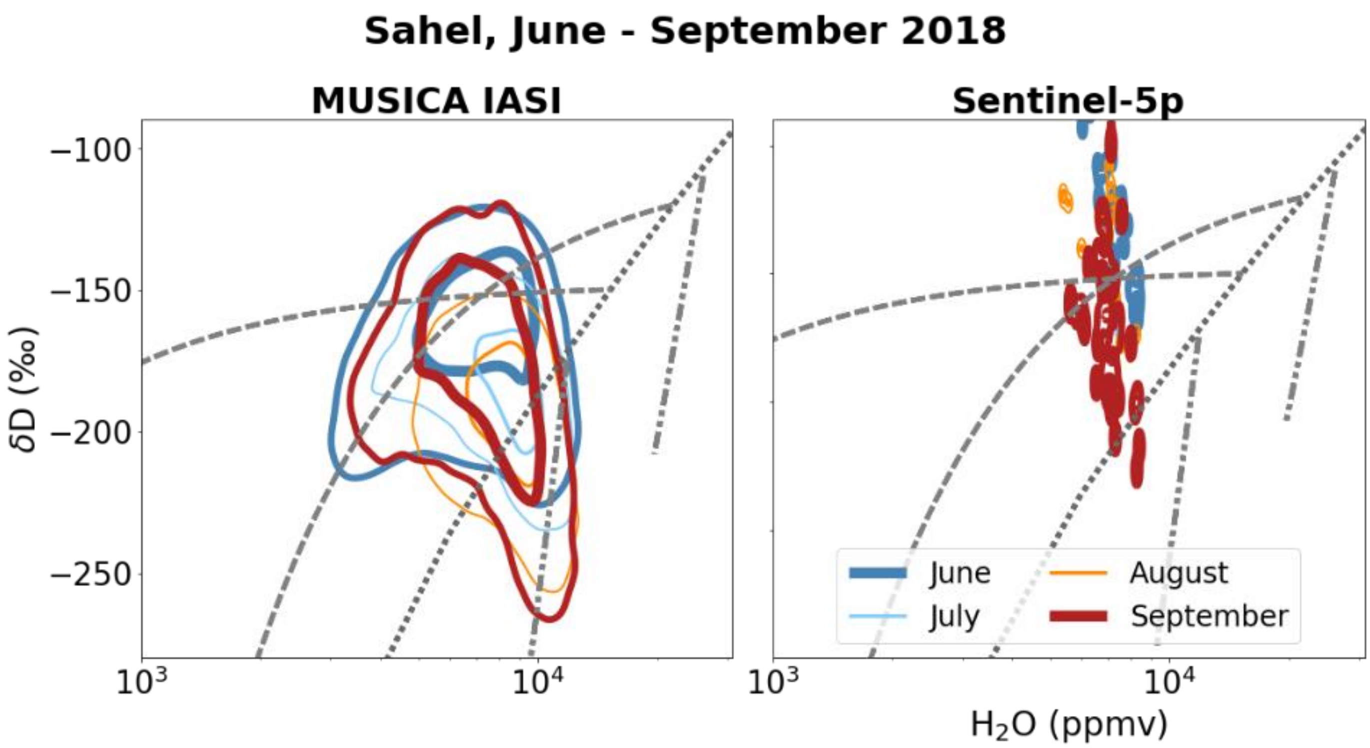

Figure 21: Quality-filtered MUSICA IASI and Sentinel-5P/TROPOMI data showing the evolution of the {H_2O,δD} distribution over the Sahel during the Monsoon period in 2018.

6.2.3 {H_2O,δD} pair signals and evaporation sources

In this section, a framework from Eckstein et al. (2018) is applied, where ICON-ART-Iso water vapour data over a target region are filtered according to the prevailing evaporative sources. This is achieved by including artificial tracers in the simulation to tag and trace water vapour that evaporates from either land or ocean surfaces. In this way, the relative fraction of each evaporative source can be determined for the chosen target region at any time.

Figure 22 shows the results of the ICON-ART-Iso simulation over West Africa during the monsoonal rainy season, when the {H_2O, δD} data over the Sahel are sorted with respect to the prevailing evaporation sources. If more than 50% of the investigated water vapour originated from land surface evaporation, it is attributed to land surface evaporation (green contours), and it is attributed to ocean surface evaporation (blue contours), if more than 50% comes from ocean surface evaporation. The separation into the two evaporative sources is performed for the three target altitude regions, i.e. the mid-troposphere, the boundary layer and the total column.

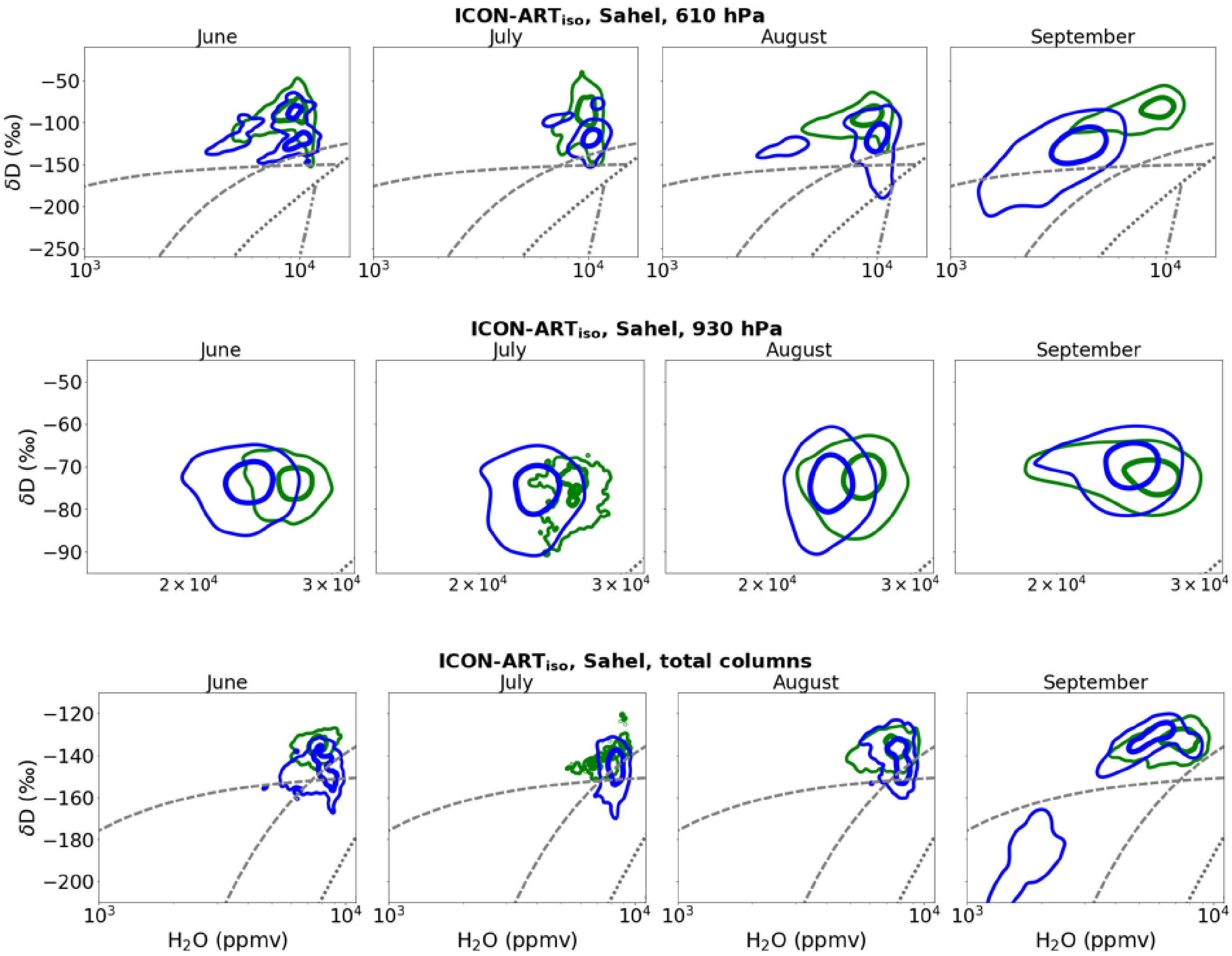

Figure 22: {H_2O, δD} data from ICON-ART-Iso over West Africa for June to September from the years 2017 to 2019, with being filtered according to the predominant evaporative source contributions. Green contours: at least 50% of the water vapour originates from land evaporation sources. Blue contours: at least 50% of the water vapour originates from ocean evaporation sources.

In the mid-troposphere, there are rather diffuse signals for the {H_2O, δD} data from land and ocean evaporation during the beginning of the monsoon season (June and July), but with the monsoon conditions evolving and strengthening, more distinct signals develop. In particular during August, a clear separation between the {H_2O, δD} distributions from land and ocean evaporation becomes apparent. Whereas the water vapour from land evaporation is mixed from rather local sources into the Sahel, the southerly monsoon winds transport water vapour evaporated from the Tropical Atlantic into the Sahel, where they initiate the monsoon convection and through rain condensation and evaporation lead to enhanced depletion in δD along the Super-Rayleigh line. In September, when the overall monsoon circulation is weakening, on the one hand the evaporation from local land surface remains unchanged, but on the other hand, the contribution from the Tropical Atlantic reduces and instead extratropical ocean sources are gaining importance again through the large-scale transport from the subtropics. For instance, water evaporates over the North Atlantic and the Mediterranean Sea and along its tropospheric transport it dries due to condensation and dry mixing with the environment, and eventually, when reaching the Sahel, it thereby creates dry signals in H_2O and δD following the mixing lines (compare blue contours in 610 hPa during September in Fig. 22). This means that the distinct {H_2O, δD}-pair distributions observed in the free troposphere for different evaporation sources is largely due to the different large scale transport regimes. In contrast, in the boundary layer persistent structures appear throughout the monsoon period. For both evaporative sources, high values in H_2O and δD appear, with less variability, as large-scale dynamics are less important in near-surface layers. However, Fig. 22 suggests the hypothesis that there is an impact of the so-called continental recycling (Galewsky et al., 2016): When water vapour from ocean surfaces are transported over land areas, condensation and rain out feeds water into the land surface, where, in turn, it poses a source for evaporation. The evaporative water again fosters condensation and rain out, what leads to the so-called recycling of water. However, all these processes have a depleting effect on δD, such that a gradual depletion in δD from the ocean evaporative source to the continental centre develops. In Fig. 22, this phenomenon can be assumed to explain the distributions in the boundary layer: Due to shorter transport distances, the water vapour from local surface evaporative sources shows higher H_2O contents compared to water vapour from marine sources, however, this increase in H_2O does not go along with an increase in δD. In September, even a drop in δD of the land evaporation contribution can be observed.

Finally, the total column again represents a mixture of the observed signals from the other two target layers. During July and August, the enhanced depletion of ocean evaporation water is apparent similar to the mid-troposphere, whereas the dry mixing signals of the ocean evaporation water in the mid-troposphere during September are only weakly reflected in the total column. Instead, the total column shows the depletion due to continental recycling as observed in the boundary layer.

6.3 Impact in the context of data assimilation

Here, we present first results testing the impact of assimilating S5P and/or IASI δD and specific humidity (q) on the meteorological analyses with an Observation System Simulation Experiment (OSSE). Note, an OSSE is an idealized experiment and the here derived results are more optimistic than these will be when assimilating the real data. For the real experiments similar results to the ones derived here with the OSSE can be expected, but with somewhat lower improvements. Nevertheless, these idealized experiments are quite helpful for deriving a first idea of the impact of data assimilation and thus help to derive the optimal set-up for the assimilation experiment with the real data.

In previous studies the impact of the assimilation of the MUSICA IASI δD and/or q data additional to conventional observations on the meteorological analyses and weather forecast has already successfully been assessed with an OSSE on a global scale (Toride et al., 2021) and in the tropics (Khosrawi et al., 2021). In Toride et al. (2021) idealized assimilation experiments were performed assimilating either δD or q as well as assimilating both, δD and q, together in the mid-troposphere. Thereby, they found that for the assimilation of IASI q higher improvements are derived than for the assimilation of IASI δD, however the assimilation of both δD and q lead always to the highest improvement indicating that isotopes hold different aspects of information than water vapour (Galewsky et al., 2016).

Similar to the assimilation experiments presented in Toride et al. (2021) further OSSEs were performed to investigate the impact of assimilating S5P δD and/or q data and MUSICA IASI q and δD and the combination of MUSCIA IASI and S5P data together. Here, we will present and compare the results of five OSSEs assimilating additional to conventional observations (1) SP5 δD columns, (2) S5P q columns, (3) S5P δD and q columns, (4) IASI δD and q at 4. 2 km and (5) S5P δD and q columns together with IASI δD and q at 4. 2 km. Note, in contrast to Toride et al. (2021) were the spatially resampled conventional observations from PREBUFR were assimilated, here a reduced number of conventional observations (due to the additional temporal sampling) has been assimilated. The performance of the S5P assimilation experiments have been assessed for the whole tropics (latitude band 10° S to 10°N) and for Africa (10°S to 10°N and 30°W to 60°E), but in the following only the results for the tropics are shown.

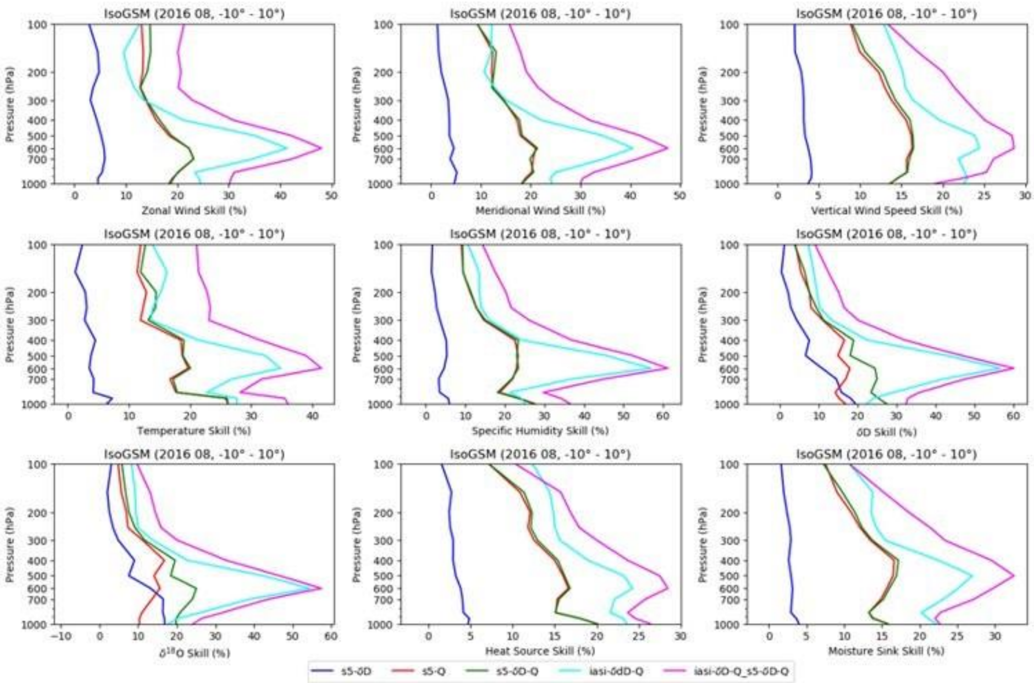

Figure 23: Temporally and spatially (tropics 10°S to 10°N, August 2016) averaged vertical profiles of the skill, showing the improvement in percent for the different assimilation experiments: S5P-δD (dark blue), S5P-q (red), S5P-δD-q (green), IASI-δD-q (light blue) and SP5-δD-q-IASI-δD-q (magenta).

The performance of the assimilation experiments is assessed using the RMSD skill. The RMSD skill gives the improvement in percentage of the assimilation experiment respective to the reference assimilation experiment (CTRL). The RMSD skill is calculated as follows:

$$Skill = \frac{RMSD_{CTRL} - RMSD}{RMSD_{CTRL}} \cdot 100, \tag{5}$$

where CTRL denotes the assimilation run with the (reduced) conventional observations.

Figure 23 shows the results for the tropics. Shown are the spatially (10°S to 10°N) and temporally (August 2016) averaged vertical profiles of the skill for the five OSSEs. The assessment has been made for the following meteorological parameters: zonal wind (u), meridional wind (v), vertical velocity (w), temperature (T), specific humidity (Q), the isotopes δD and δ18O, heat source (Q1) and moisture sink (Q2). For all meteorological parameters about 5% improvement are derived when only Sp5 δD is assimilated. Higher improvements (20-40%) can be derived when S5P q or S5P δD and q are assimilated. The highest improvements of about 35-45% are derived when S5P δD and q are assimilated together with MUSICA IASI δD and q. While for S5P δD the improvement is almost the same for all pressure levels up to 100 hPa, the improvement for S5P q and SP5 q and δD decreases with altitude and the ones for IASI δD and q and IASI-δD-q-S5P-δD-q show the highest improvement in the mid-troposphere.

Approximately the same improvements are found for the assimilation experiments with S5P q and S5P δD and q, thus the assimilation experiments show little additional value when δD is assimilated additional to q in contrast to the MUSICA IASI experiments presented in Toride et al. (2021). However, this is the case for the tropics, but not for other regions such as e.g., Africa. For Africa we find higher improvements for the assimilation of S5P δD and q than for the assimilation of S5P q. Also when the assimilation is assessed globally higher improvements are found for S5P δD and q than for Sp5 q. Possible reasons for that we derive here somewhat different result than in Toride et al. (2021) may be due to the fact that for S5P columns have been assimilated and these hold less detailed information on specific humidity processes than if δD is assimilated on a certain altitude and also the coarse resolution of the model used in these experiments is a drawback and may enhance this effect. Nevertheless, the highest improvement is found for the assimilation of S5P δD and q together with MUSICA IASI δD and q (35-45 %) showing that the assimilation of data from both instruments may be valuable for improving meteorological analyses and weather forecast.

7 Conclusions and Outlook

In this Impact Assessment Report, we pursued four goals during the data assessment: (1) assess the ability and conditions of in-situ measurements to serve as ground-truth for satellite observations, (2) assess the insight offered by S5P total column data to supplement information available from MUSICA IASI in West Africa, and (3) a preliminary investigation in the context of data assimilation. From these partial goals, we more generally assess (4) the additional value of the S5P satellite data product compared to other data, we summarize and conclude on points 1-3 first, before deriving an assessment with regard to point (4) from the new insight gained with regard to validation within S5P+I overall. Wider implications and potential next steps are provided in Sec. 8.

(1) The ability and conditions of in-situ measurements to serve as ground-truth for satellite observations:

- Spatial and temporal scales are important factors in the comparison between satellite, in-situ, and NWP model data. The measurement location of in-situ data critically determines on what scales a meaningful comparison can be made. Hereby, local topographic effects combined with the weather situation need to be assessed for the relevant scales based on a so-called complete proxy (here, regional isotope-enabled NWP model simulations).
- Cloud cover, shifts in weather pattern, and varying topography can limit comparison efforts, as was the case for the Alpine region investigated during L-WAIVE. Apart from such adverse effects, these factors create variability of the signal, and thus provide the structure in the data set that enables meaningful interpretation. To the extent feasible, measurements should be planned to balance these counteracting demands by choosing a measurement site and time period which represents the regions' isotopic variability without shortcutting on the data coverage.
- For best possible aircraft – satellite comparison, the flights and satellite overpasses should be synchronized (if possible, taking into account overall campaign objectives). This is most important in regions with a strong daily cycle in vertical δD profiles or in situations with a high temporal variability in large-scale forcings.
- The design of flight patterns for optimal in-situ comparisons is challenging, and restricted by the measurement platform and endurance, air traffic restrictions, and the weather situation. To allow for a larger degree of overlap, sampling patterns should cover horizontal scales of 50 km and more, and cover vertical levels from the ground to above about 5000 m. The ultralight aircraft employed in the L-WAIVE campaign were focused on smaller scales and boundary-layer characteristics in complex terrain. Despite the overall value of the L-WAIVE data, measurements from aircraft that cover larger horizontal scales would be more suitable for the comparisons targeted here.

- From a point of view of comparing satellite observations, it is more important to reach higher levels than to obtain a very detailed vertical resolution. Interestingly, ground-based remote sensing instrumentation, such as the δD-capable LIDARs developed during the WaVIL or LEMON (https://lemon-dial-project.eu/) projects require detailed vertical oversampling with long averaging times to enable meaningful comparisons. Therefore, detailed flights with ultralight aircraft can be an important intermediary to enable indirect satellite-LIDAR comparisons.

(2) Assessing the insight offered by S5P total column data to supplement information available from MUSICA IASI in West Africa:

- As a basis for all comparisons in the target region West Africa, we note that the large-scale circulation patterns in the Sahel region strongly vary with altitude, inducing vertical wind shear. In the free troposphere, the air mass origins are rather different from the air mass origins in the boundary layer. Such differences can strongly impact both total column and vertically resolved satellite observation products.
- The MUSICA IASI {H_2O, δD} pair data are able to capture signals well that are due to the large scale circulation in the free troposphere and signals of convective processes. The basis for this conclusion is that the {H_2O, δD} pair distribution is in accordance with Super-Rayleigh lines.
- S5P offers total integrated column data. These data reflect a mix of the different altitudes with different circulation patterns. Air masses from different origins and different transport processes determine the total column signals. Such differential advection is a substantial obstacle to the use of the S5P data for atmospheric water pathway studies in this region.
- Combining S5P with MUSICA IASI offers the potential for separating the boundary layer from the free tropospheric signals (Schneider et al., 2021b). Testing such a boundary layer isotopologue separation for our region, we found strong indications that the distribution of boundary layer {H_2O, δD}-pairs is different for an ocean or land evaporation sources.

(3) Assessing a preliminary investigation of S5P isotopologue data in the context of data assimilation:

- In the tropics, the assimilation of S5P q and S5P δD and q combined leads to almost the same improvement. In other words, little additional gain is derived from assimilating column δD additionally to column q. This limited gain indicates that column δD holds less detailed information on moisture processes than if δD observations are obtained for a specific altitude in the mid-troposphere.
- The assimilation of both IASI δD and q additionally to S5P δD and q leads to the highest improvement (35-45%) for all meteorological parameters (tropics and Africa). This

improvement shows the potential for the assimilation of data from both instruments together for improving meteorological analysis and thus weather forecasts.
- As indicated by Fig. 15 comparing ICON-ART-iso with IMERG, for capturing the precipitation and thus latent heating pattern correctly a higher horizontal resolution as the one used here for the data assimilation could be beneficial (remember, the data assimilation experiment with IsoGSM was performed with a horizontal resolution of 200 x 200 km). Another option would be to repeat the data assimilation experiments with a higher number of ensemble members or to apply the relaxation-to-prior method (RTPS) as done in Toride et al., 2021). We expect that assimilation experiments using a higher model resolution and/or more ensemble members and/or applying the RTPS method might give different results.

(4) Overall assessment and new insight gained during the validation of isotopologue data from S5P:

The isotopologue retrieval from S5P provides spatial and temporal coverage that is highly useful for deciphering the interrelation between weather situations and the isotopic state of atmospheric water vapour, in particular in combination with other satellite products, as demonstrated from preliminary data assimilation experiments. Similar additional value became evident from the analysis of isotopic signatures in the large-scale circulation in West Africa, where a combination of the S5P data with the MUSICA product may allow to extract vertically resolved information. Vertical atmospheric differences are also a key challenge for the use of in-situ validation, which generally benefit more from high-reaching profiles than from high vertical resolution. Complex terrain influences both the correlation length scales and the vertical structure, which therefore need to be taken into account during comparison with in-situ data. Simulations with isotope-enabled NWP models are a key asset during such validation studies, and provide both larger spatial and temporal context, serve as verification target, and enable synthetic verification studies. Proceeding along the 3 main directions outlined in this impact assessment report appears as a promising avenue to maximise the impact from the S5P isotopologue data developed here.

8 Wider implications and Outlook

From the assessment of the ability and conditions of in-situ measurements to serve as ground-truth for satellite observations, we derive the following aspects that have wider implications, and that could be valuable to followed up in future work:

- The current resolution of 0.1° of the COSMO$_{iso}$ simulations provides a dataset in a similar resolution as the satellite retrievals, but misses to resolve the topography around lake Annecy. This lack in resolving the topography might lead to some short-comings in the simulation of the local convection along the Western Alps, which strongly influenced the local weather during the campaign. A higher resolution (e.g. 0.02°) COSMO$_{iso}$ simulation would help to estimate the role of the local convection on the vertical δD profiles and how they compare to the satellite overpasses
- The scale analysis presented here focuses only on δD_{pwf}. Including the dominant scales of non-isotope variables such as specific humidity, relative humidity, column water vapour or air temperature could help to relate the determined scale of δD_{pwf} to other scales.
- The focus on two weeks in June limits the applicability of the determined temporal and spatial scales to other time periods. For a more general conclusions, a scale analysis over longer time period has to be conducted, e.g. by using nudged COSMO$_{iso}$ simulations and/or by using other variables such as specific humidity in reanalysis data for a climatological perspective.
- The scales determined using COSMO$_{iso}$ simulations might differ from spatial scales in S5P-TROPOMI retrievals. To clarify this aspect, a scale analysis could be performed using the existing S5P retrievals. The unregular availability in time and space of the TROPOMI data causes some challenges for statistical analysis. These could be solved by interpolation of missing values or decreasing the spatial resolution.
- Further statistical measures could be applied to better characterise the spatial and temporal scales of δD. For example, changing the temporal resolution of the δD time series allows to filter specific modes of variability.
- Further comparison studies using in-situ vertical profiles should be performed from additional field observations that have recently become available from the LEMON project in Aubenas, France during September 2021. To the extent possible, the results from this IAR will be communicated to researchers conducting upcoming field experiments, such as the ISLAS campaign near Kiruna during March 2022, where measurements near FTIR site Sodankyla can be coordinated with a satellite overpass. Measurements with larger aircraft, such as during the LEMON validation campaign in 2022 or 2023 may allow to access larger horizontal and vertical scales.

From the assessment regarding the supplement information available from MUSICA IASI in West Africa, and a preliminary investigation in the context of data assimilation, we derive the following aspects that have wider implications, and that could be valuable to followed up in future work:

- Improvements need to be made in terms of the S5P quality-filtering (at least over West Africa), where currently a large amount of data is filtered out.
- If combined with MUSICA IASI, the S5P data can point towards other vertical layers than MUSICA IASI alone. This enables to obtain information about different water vapour processes and sources. However, the synergetic combination of S5P and MUSICA IASI, which has already been developed and validated for CH4 (Schneider et al., 2021b), needs to be adopted to water isotopologues.
- To better constrain the benefit that the assimilation of the S5P δD and q together with IASI δD and q could have for the meteorological analyses and weather forecast, further assimilation experiments with synthetic as well as real data using a higher model resolution would be needed.

Appendix

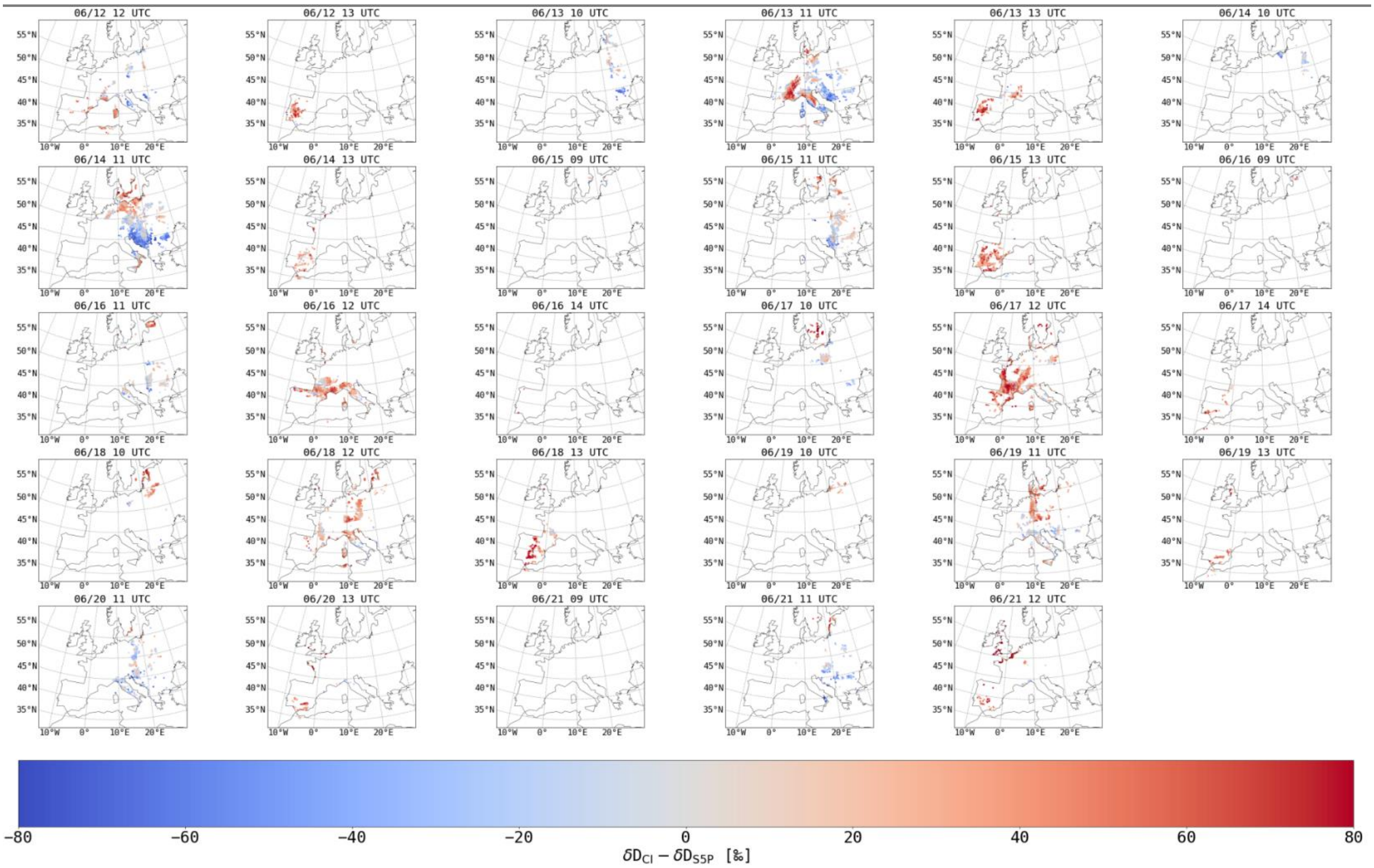

Figure A1: Scatteplots of the difference between total column δD from COSMO$_{iso}$ simulations and S5P retrievals for collocated satellite overpasses.

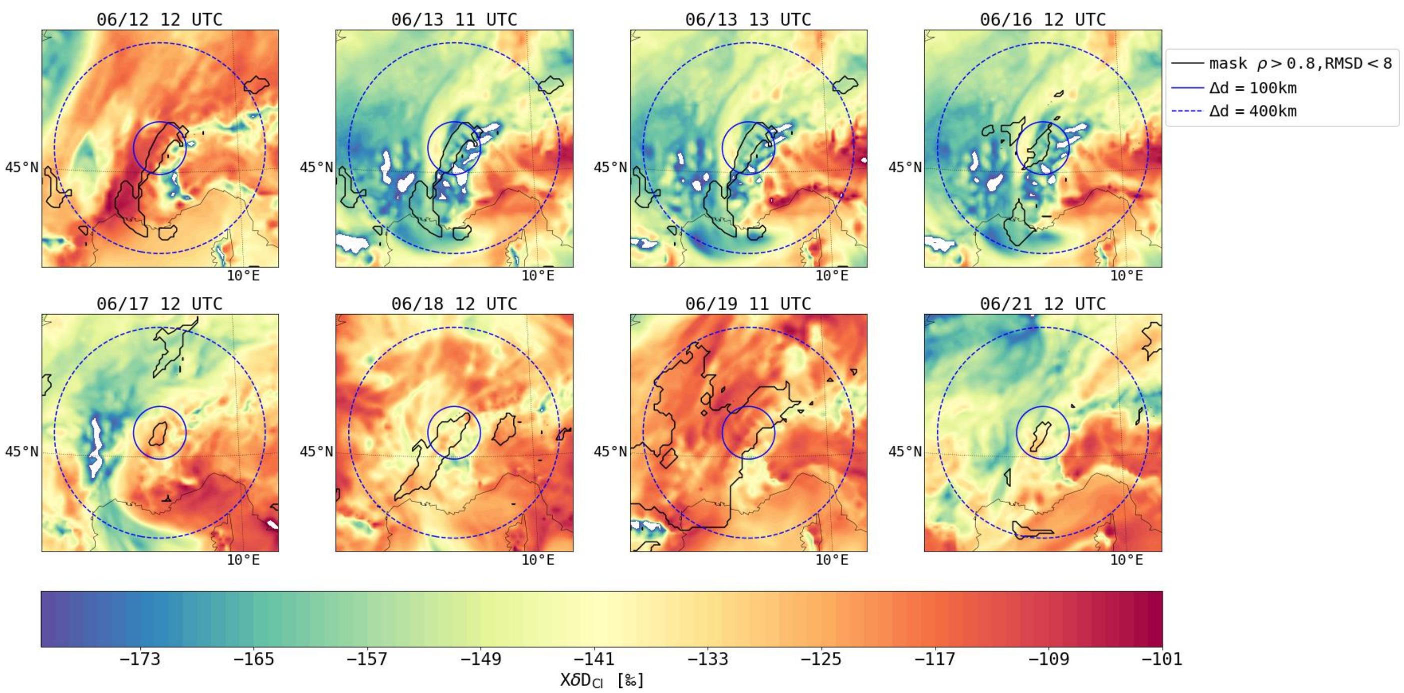

Figure A2: XδD in COSMO$_{iso}$ for time steps collocated with satellite overpasses. Black contours show the daily masks based on ρ and RMSE. Blue solid contours mark 100 km distance from Annecy, dashed blue contours 400 km distance.